JGR Space Physics

RESEARCH ARTICLE
10.1029/2023JA031631

Special Section:
Fifteen Years of THEMIS Mission

Energetic Electron Flux Dropouts Measured by ELFIN in the Ionospheric Projection of the Plasma Sheet

Yangyang Shen[1], Anton V. Artemyev[1,2], Andrei Runov[1], Vassilis Angelopoulos[1], Jiang Liu[1,3], Xiao-Jia Zhang[1,4], James M. Weygand[1], Jiashu Wu[1], Ethan Tsai[1], and Colin Wilkins[1]

[1]Department of Earth, Planetary, and Space Sciences, University of California, Los Angeles, Los Angeles, CA, USA, [2]Space Research Institute of Russian Academy of Sciences, Moscow, Russia, [3]Department of Atmospheric and Oceanic Sciences, University of California, Los Angeles, Los Angeles, CA, USA, [4]Department of Physics, University of Texas at Dallas, Richardson, TX, USA

Abstract Low-altitude observations of magnetospheric particles provide a unique opportunity for remote probing of the magnetospheric and plasma states during active times. We present the first statistical analysis of a specific pattern in such observations, energetic electron flux dropouts in the low-altitude projection of the plasma sheet. Using 3.5 years of data from the ELFIN CubeSats we report the occurrence distribution of 145 energetic electron flux dropout events and identify characteristics, including their prevalence in the dusk and premidnight sectors, their association with substorms and enhanced auroral activities, and their correlation with the region-1 (R1) field-aligned current region. We also investigate three representative dropout events which benefit from satellite conjunctions between ELFIN, GOES, and THEMIS, to better understand the magnetospheric drivers and magnetic field conditions that lead to such dropouts as viewed by ELFIN. One class of dropouts may be associated with magnetic field mapping distortions due to local enhancements and thinning of cross-tail current sheets and amplification of R1 field-aligned currents. The other class may be associated with the increase in perpendicular anisotropy of magnetospheric electrons due to magnetic field dipolarizations near premidnight. These plasma sheet flux dropouts at ELFIN provide a valuable tool for refining magnetospheric models, thereby improving the accuracy of field-line mapping during substorms.

Plain Language Summary Low-Earth Orbit (LEO) observations of magnetospheric particles can sometimes provide critical information on complex high-altitude processes that are challenging to access. Here we introduce a novel type of LEO particle measurement: energetic electron flux dropouts in the low-altitude projection of the plasma sheet. These particle observations may prove valuable for remotely probing magnetospheric configurations during geomagnetically disturbed times. Utilizing 3.5 years of data from the ELFIN CubeSats, we conduct the first statistical analysis of these flux dropout events. Our findings reveal that they predominantly occur in the dusk and premidnight magnetic local time sectors during substorms, and exhibit a well-defined relationship with the large-scale field-aligned current region. We also examine three representative dropout events to gain a deeper understanding of the magnetospheric drivers and magnetic field conditions that lead to such dropouts at low altitudes. These plasma sheet flux dropouts at ELFIN provide a valuable tool for refining magnetospheric models, consequently enhancing the accuracy of field-line mapping during disturbed times.

Key Points:

- We report statistical observations of energetic electron flux dropouts at the low-altitude extent of the plasma sheet by ELFIN
- Flux dropouts occur preferentially at dusk and premidnight and are collocated with R1 FAC poleward of the electron isotropy boundary
- Two types of magnetospheric drivers of ELFIN flux dropouts are discussed by analyzing three conjunction events with GOES and THEMIS

Supporting Information:

Supporting Information may be found in the online version of this article.

Correspondence to:

Y. Shen,
yshen@epss.ucla.edu

Citation:

Shen, Y., Artemyev, A. V., Runov, A., Angelopoulos, V., Liu, J., Zhang, X.-J., et al. (2023). Energetic electron flux dropouts measured by ELFIN in the ionospheric projection of the plasma sheet. *Journal of Geophysical Research: Space Physics*, *128*, e2023JA031631. https://doi.org/10.1029/2023JA031631

Received 22 APR 2023
Accepted 4 SEP 2023

1. Introduction

An adequate description of global and regional magnetospheric magnetic field configurations is critical to many aspects of magnetospheric physics, such as modeling radiation belts dynamics (e.g., Ni, Thorne, Shprits, et al., 2011; Orlova & Shprits, 2010; Turner et al., 2012), simulating particle acceleration and transport (e.g., Birn et al., 2012; Gabrielse et al., 2017; Shen et al., 2022), and linking complex and dynamic physical processes along field lines between the ionosphere and the magnetosphere (Kubyshkina et al., 2019; Sergeev, Angelopoulos, & Nakamura, 2012). Mapping from the ionosphere to the magnetosphere is a long-standing and vexing problem. This mapping becomes very unstable during active periods of storms and substorms (Kubyshkina et al., 2011), when the magnetic field topology undergoes rapid and major reconfigurations of stretching and dipolarization (Angelopoulos, Artemyev, et al., 2020; Angelopoulos, McFadden, et al., 2008; Stephens & Sitnov, 2021; Stephens et al., 2023; Tsyganenko & Sitnov, 2005). Kubyshkina et al. (2011, 2019) demonstrated that variability

of ionospheric footprints of spacecraft in the plasma sheet was on average ∼1°–∼4° in latitude but can reach 10° in extreme cases. In addition, even small deviations in latitude can lead to large errors (often >10 R_E, R_E is the Earth radius) in the estimate of radial distances in the equatorial projections.

Different approaches have been used to predict magnetospheric configurations and provide adequate magnetic field mapping from the ionosphere to the magnetosphere. One common approach fits hundreds of thousands of spacecraft magnetic field measurements at different locations and times and under different solar wind driving (Stephens et al., 2016, 2019, 2023; Tsyganenko, 1995, 2002; Tsyganenko & Andreeva, 2016; Tsyganenko & Sitnov, 2005; Tsyganenko et al., 2021). These empirical models are built on blocks describing different magnetospheric current systems (Ganushkina et al., 2018) and provide a valuable average representation of magnetic fields. Owing to their statistical nature, they cannot account (barring further case-by-case fine-tuning) for details of magnetic variations during substorms. Built upon empirical models, adaptive modeling assimilates instantaneous actual magnetic field measurements from a handful of available magnetospheric satellites at some particular time (Kubyshkina et al., 2009, 2019). Although adaptive models provide relatively more accurate magnetic field topology and mapping, a systematic application of this approach is hindered by the scarcity and uneven coverage of magnetospheric observations. In addition, empirical first-principle and global numerical magnetic field models also exist for dedicated applications in certain regions and at specific times (e.g., Artemyev et al., 2021; Yue et al., 2013, 2015, and references therein).

Another approach, often complementary to the aforementioned, uses ground-based or low-altitude observations of plasma characteristics to remotely probe magnetospheric regions and magnetic field topology. For example, auroral images measured from the THEMIS ground-based all-sky imagers (ASIs) have been used to identify key boundaries and onset times of substorms (Donovan et al., 2008; Gillies et al., 2019; Lyons et al., 2013; Mende et al., 2007; Sergeev, Nishimura, et al., 2012). Low-energy (<30 keV) particle measurements from low-altitude spacecraft (such as DMSP) have been used to identify the polar cap (or open/closed field line) boundary based on energy-latitude dispersion of polar rain (<1 keV diffusive electrons in the polar cap) precipitation near this boundary (Gallardo-Lacourt et al., 2022; Wing & Zhang, 2015; Winningham & Heikkila, 1974). Similar dispersion in low-energy ions, also termed cusp ion steps, have been utilized to identify the cusp proper that is linked to the dayside magnetopause reconnection region (Heikkila & Winningham, 1971; Smith & Lockwood, 1996; Walsh et al., 2021). Newell and Meng (1992) used tens of thousands of individual particle precipitation measurements by the low-altitude satellites of DMSP to construct an ionospheric map into various dayside magnetospheric regions, such as the dayside cusp, lower-latitude boundary layer, mantle, plasma sheet, and polar rain, based on plasma precipitation characteristics with energies below ∼30 keV. Higher-energy (>∼30 keV) proton and electron isotropy boundaries (IB) have also proven to be robust geophysical parameters to probe instantaneous magnetospheric configurations and to constrain and validate magnetic field mapping (Dubyagin et al., 2002; Kubyshkina et al., 2009; Newell et al., 1998; Sergeev et al., 1993).

As the name implies, the isotropy boundary is the ionospheric latitudinal boundary separating adiabatic and chaotic regimes of particle motion in the projected equatorial magnetotail (Buchner & Zelenyi, 1989; Sergeev & Tsyganenko, 1982). The IB location is determined by the ratios of the minimum magnetic field curvature radius (R_c) over the maximal particle gyroradius (ρ_m) in the current sheet (Sergeev et al., 1983). Poleward of the IB, particle precipitating-over-perpendicular flux ratios are close to 1, that is, distributions are isotropic. Such isotropic precipitation is attributed to field-line curvature (FLC) scattering in the current sheet (Buchner & Zelenyi, 1989; Liang et al., 2013). The theoretical threshold ratio for FLC scattering to occur was suggested to be $\kappa^2 \sim R_c/\rho_m \sim 8$ (Sergeev et al., 1993), although modifications of this threshold were reported (Delcourt et al., 1995; Dubyagin et al., 2018; Ilie et al., 2015). For a given value of κ near the threshold, the effects of FLC scattering are strongest at very small pitch angles but become negligible at large pitch angles (Delcourt et al., 1995). Because R_c increases rapidly with decreasing radial distance in the magnetotail, the minimum FLC-induced precipitating particle gyroradius, or the minimum energy, increases with decreasing latitude when observed by low-altitude spacecraft. Thus, the energy-latitude dispersion of the IB can be used to infer the magnetic field topology in the equatorial magnetosphere, especially during substorms when instantaneous magnetic field configurations are of interest (Kubyshkina et al., 2011).

During substorms, magnetic field distortions are expected to be exacerbated by several intensified, dynamic current systems (Ganushkina et al., 2010). For example, substorm magnetotail thin current sheets often intrude the inner magnetosphere (Artemyev et al., 2019; Petrukovich et al., 2007; Runov et al., 2021), causing extreme

stretching of magnetic field configuration at near-Earth space (Artemyev, Angelopoulos, et al., 2022; Artemyev, Neishtadt, et al., 2022). Such stretching and current sheet intensification, either during the growth phase or during recovery phases of multiple substorms, may produce enhanced FLC scattering and/or lead to depleted energetic fluxes in spacecraft observations due to the spacecraft exiting to the lobe region (Baker & McPherron, 1990; Fennell et al., 1996; Huang et al., 2003).

Also, the large-scale Region-1 (R1) and Region-2 (R2) field-aligned currents (FACs) are amplified during substorms (Iijima & Potemra, 1978; Yang et al., 2012). They can twist field lines in their local neighborhood, mostly in Geocentric Solar Magnetospheric (GSM) B_y, but also in B_x and B_z (Tsyganenko & Stern, 1996). A great part of intensified FACs near pre-midnight and midnight is linked to the substorm current wedge (SCW) system (Birn & Hesse, 2013; Kepko et al., 2014; McPherron et al., 1973). The classical view of the current wedge consists of part of the cross-tail current that diverts to the ionosphere during the substorm, where horizontal westward electrojets (or Hall currents) flow and are associated with the downward FAC on the dawnside and the upward FAC on the duskside. Around its equatorial center meridian, significant B_z enhancements are observed to be associated with the magnetic flux pileup due to dipolarizations (Birn & Hesse, 2013; Gabrielse et al., 2019; Yang et al., 2012). Consistent with equatorial magnetic signatures, the ground-based magnetometers at mid-latitudes reveal positive north-south (H component) magnetic perturbations near the center local time and east-west (D component) magnetic perturbations with polarities in agreement with FACs on either sides. These FAC directions are the same as for the large-scale R1 FAC system.

The equatorial magnetic field B_z variations often result in adiabatic acceleration or deceleration of particles and formation of anisotropic particle distributions (Apatenkov et al., 2007; Birn et al., 1999, 2022; H. S. Fu et al., 2012; Runov et al., 2013; Turner et al., 2016). In the midtail ($R > 10\ R_E$) region, for example, H. S. Fu et al. (2012) examined pitch-angle distributions (PADs) of >40 keV electrons associated with dipolarization fronts using Cluster observations. They found that perpendicular (or pancake-type) distributions appear mainly inside the growing flux pileup region (FPR), whereas field-aligned (or cigar-type) distributions occur mainly inside a decaying FPR. The pancake-type distribution is typically associated with betatron acceleration due to magnetic field increases, whereas the cigar-type is typically associated with Fermi acceleration due to contracting field lines (Birn et al., 1999). Runov et al. (2013) used multi-point observations from THEMIS to show that electron distributions with energies of <30 keV at dipolarization fronts are mostly pancake-type closer to the local neutral sheet and cigar-type at higher latitudes. Combining MHD and test-particle simulations, Birn et al. (2014) showed an approximately consistent picture with Runov et al. (2013), although at energies >30 keV a dominance of perpendicular anisotropies was seen in the simulations.

In the near-Earth ($R \lesssim 10\ R_E$) region, Baker et al. (1978) reported a consistent sequence of variations of the energetic (30–300 keV) electron anisotropy based on ∼100 events. They found that cigar-like parallel electron distributions, prevalent during the substorm growth phase, will give way to pancake-shaped perpendicular electron distributions after substorm onsets. Smets et al. (1999) investigated Interball-Tail observations of the electron PADs at 10 keV following the dipolarization phase of a substorm. They found that anisotropic electron PADs evolve from highly beam-like (or cigar-type) to highly pancake-like as the spacecraft traversed decreasing L-shells from $L \sim 11$ to $L \sim 7$. Assuming conservation of first and second adiabatic invariants of electrons in the model magnetic configurations, they used Liouville's theorem to model electron evolution and found that these spatial distributions of electron PADs are consistent with betatron and Fermi acceleration due to magnetic field topological changes at different radial positions during the substorm. Based on a detailed analysis of energetic electron injections observed by MMS at ∼10 R_E in the dusk/pre-midnight sectors, Turner et al. (2016) demonstrated that electrons are accelerated cumulatively by a series of impulsive magnetic dipolarization events to hundreds of keV, and that >10 keV electrons primarily experience betatron acceleration that leads to dominant perpendicular anisotropy.

The magnetospheric magnetic field variations and anisotropic electron distributions observed during substorms will likely also reveal themselves in low-altitude spacecraft observations as some particular patterns of energetic electron precipitation. Herein, based on observations by the polar-orbiting ELFIN CubeSats at low altitudes (∼450 km), we report a new feature of energetic (>50 keV) electron precipitation, that is, energetic electron flux dropouts in the low-altitude projection of the plasma sheet. Such energetic electron flux dropout events exhibit a well-defined statistical relationship with large-scale R1 and R2 FACs, and are primarily observed in the dusk and pre-midnight sectors during substorms. These observations may be useful to remotely probe magnetospheric magnetic field and plasma states during substorms.

2. Instrumentation and Data

We use energetic electron measurements from the twin ELFIN CubeSats (ELFIN-A, ELFIN-B; or ELA, ELB) at altitudes of ∼450 km (Angelopoulos, Tsai, et al., 2020). The energetic particle detector for electrons (EPDE) onboard ELFIN measures electrons from 50 keV to ∼6 MeV in 16 energy channels and PADs in 16 (full-spin) angular sectors with a resolution (FWHM) of ∼22.5° every 3 s. The energetic particle detector for ions (EPDI) measures energetic ions from 50 keV to ∼5 MeV with the same pitch-angle resolution with electrons. The local magnetic field is nominally within 15° of the spin plane, which allows ELFIN's detectors to resolve precipitating, backscattered, and trapped electron and ion fluxes (see Angelopoulos et al., 2023). The fluxgate magnetometer (FGM) instrument, placed on a ∼75 cm boom, measures vector magnetic fields with a sampling rate of 10 per spin period (3 s), nominally covering the frequency range from DC to Nyquist frequencies of 5 Hz with <0.3 nT/sqrt(Hz) noise at 1 Hz (Angelopoulos, Tsai, et al., 2020). We will use only spin-resolution (spin-averaged) magnetic field data to identify large-scale R1/R2 currents.

We examine both ELA and ELB energetic electron data during the period from April 2019 to September 2022 to provide a statistical distribution of energetic flux dropout events at the low-altitude extent of the plasma sheet. For each event to be selected into our database during this period, regardless of whether or not the flux dropout event occurs, ELFIN must have good-quality flux measurements covering both the radiation belt ($L > \sim 4$) and the plasma sheet for a significant portion (extending to at least $L \sim 12$). Poor quality measurements can obscure identification of flux dropout events, such as those with too many telemetry gaps, significant solar energetic particle contamination, and have been excluded from overall statistics. In total, 145 plasma sheet flux dropout events have been identified at nightside within the magnetic local time (MLT) of 17–6 hr. Of these, 28 events have good magnetic field measurements to identify the relation with large-scale R1/R2 currents. The magnetic field measurements for many other events are still under active calibration.

Our general event identification criteria are: (a) Flux dropouts with electron integral trapped energy fluxes $<\sim 2 \times 10^4$ keV/cm^2-s-str over the energy range of 50–630 keV have been observed poleward of the outer radiation belt and within the plasma sheet; (b) Both the poleward and equatorward sides of the flux dropout region must have integral trapped fluxes $\gg 2 \times 10^4$ keV/cm^2-s-str; (c) The poleward extent of the plasma sheet trapped fluxes must be continuous without significant gaps for at least 10 spin periods (∼30 s), to ensure the presence of a well-defined plasma sheet region; (d) The inner edge of the electron plasma sheet is typically identified through the electron isotropy boundary (IB) or, in its absence, by trapped fluxes that exhibit maximum energies of mostly below ∼300 keV; (e) Consecutive ELA and ELB measurements of similar flux dropouts within ∼45 min are considered as a single event; (f) Energetic flux dropouts observed equatorward of the IB in the outer radiation belt were excluded from our study (Onsager et al., 2002; Shprits et al., 2006; Turner et al., 2012). The event list including the association with R1/R2 FACs is provided in Supporting Information S1.

Apart from ELFIN measurements, we also use data from the GOES16, GOES17, and THEMIS spacecraft when they are in conjunction with ELFIN in several of our events. These conjunction events are merely presented as examples to illustrate the potential linkage between magnetospheric magnetic field and plasma states and plasma sheet flux dropouts in the ionosphere. We will use the magnetic field measurements (at 1-min resolution) from the GOES satellites at the geostationary position ($R \sim 6.6\ R_E$) (Lotoániu et al., 2020). From the THEMIS spacecraft, we use electron data in the energy range from ∼10 eV to 25 keV measured by the Electrostatic Analyzers (ESAs) (McFadden et al., 2008) and from 25 keV to ∼900 keV measured by the Solid State Telecope (SST) instrument (Angelopoulos, Sibeck, et al., 2008; Runov et al., 2015), and DC vector magnetic field at spin resolution (∼3 s) measured by the Fluxgate Magnetometers (FGM) (Auster et al., 2008). In addition, background electron densities are inferred from spacecraft potentials (Bonnell et al., 2008), and electron and ion temperatures are obtained from combined ESA and SST measurements.

Furthermore, we use ground-based magnetometers to identify the relative locations of ELFIN measurements with respect to ionospheric large-scale currents for our conjunction events (Engebretson et al., 1995; Mann et al., 2008; Russell et al., 2008). We will also use a well-developed and validated magnetometer data product of 2D ionospheric currents using the spherical elementary current system (SECS) method for our conjunction events (Amm & Viljanen, 1999; Weygand et al., 2011). Dynamic maps of equivalent ionospheric currents (EICs, horizontal currents) and current amplitudes (SECAs, a proxy for FACs) allow identification of both the large-scale R1/R2 currents and the substorm current wedge associated with magnetic dipolarizations (e.g., McPherron &

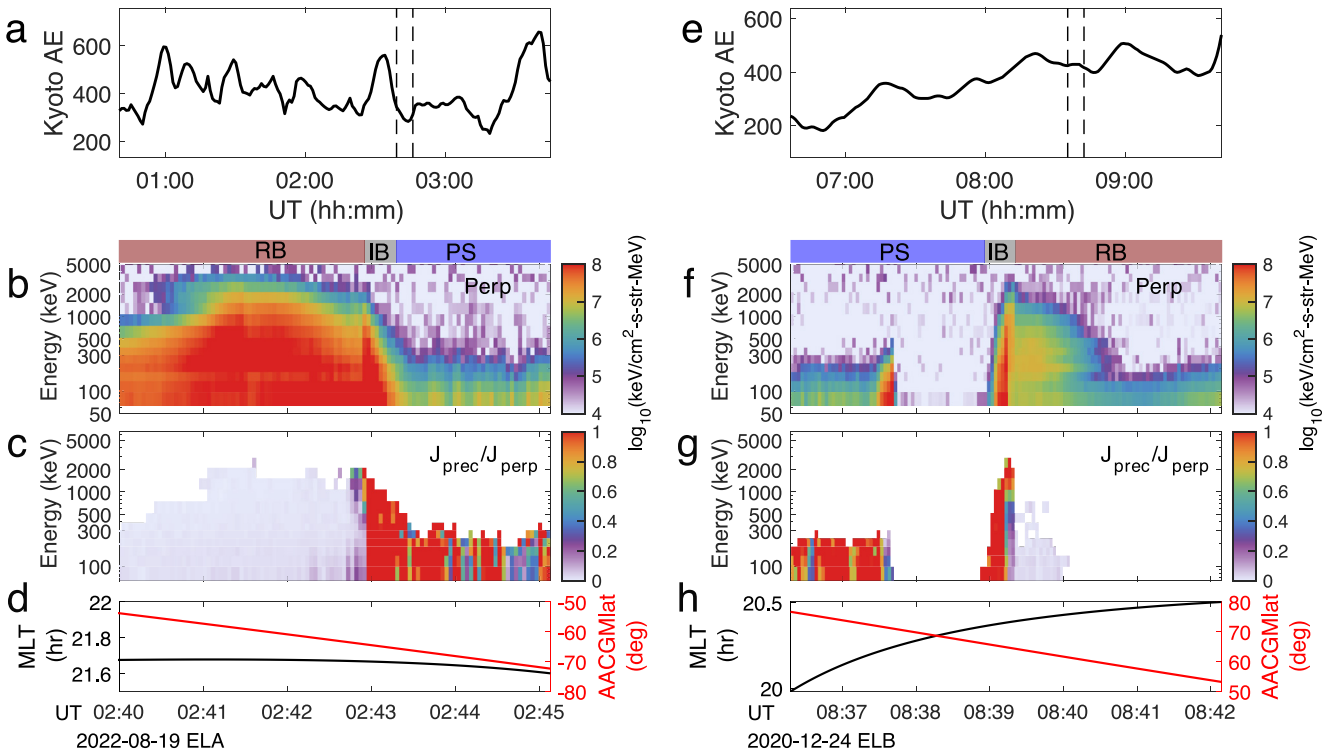

Figure 1. Examples of radiation belt (RB) and plasma sheet (PS) energetic electron measurements by ELFIN, displaying events without (a–d) and with (e–h) plasma sheet flux dropouts on 19 August 2022 and 24 December 2020, respectively. The top-row (a, e) shows time variations of AE, with the intervals of ELFIN electron measurements indicated between the dashed lines. The second row (b, f) shows perpendicular electron flux energy-time spectrograms. The RB, isotropy boundary (IB), and PS regions are indicated at the top. The third row (c, g) shows precipitating-over-trapped electron flux ratios. The last row (d, h) shows MLT and magnetic latitude (*Mlat*) in the Altitude-Adjusted Corrected Geomagnetic (AACGM) coordinates for the two events.

Chu, 2017; Panov et al., 2016). Lastly, we use both the SML and AE indices to support our identification of substorms or enhanced auroral activities (Gjerloev, 2012; Newell & Gjerloev, 2011).

3. Observations

3.1. An Example of ELFIN Flux Dropout in the Plasma Sheet

Figure 1 depicts two separate events of energetic electron measurements by ELFIN-A and ELFIN-B when the spacecraft traversed the high-latitude ionosphere near 02:40 UT on 19 August 2022 and near 08:40 UT on 24 December 2020, respectively. Electron fluxes from the radiation belt (RB) and from the plasma sheet (PS) were both observed at similar MLTs near premidnight (20–22 hr) and with similar AE levels (~400 nT). The latitudinal boundary that demonstrates isotropic fluxes at energies dispersively decreasing with increasing latitude near the outer edge of the radiation belt bespeaks an electron isotropy boundary (IB), which was observed in both events (Figures 1c and 1g). This IB location demarcates the anisotropic precipitation from the radiation belt and isotropic precipitation from the plasma sheet. While the event on the left displays continuous perpendicular and precipitating electron fluxes (Figures 1b and 1c), as ELFIN-A transected the radiation belt and the plasma sheet regions, the event on the right demonstrates a complete electron perpendicular and precipitating flux depletion above 50 keV, as ELFIN-B passed by the poleward edge of the IB and traveled into the plasma sheet region (Figures 1f and 1g). Electron fluxes in the dropout region are below EPDE sensitivity, consistent with zero. Further poleward of the flux dropout region, a wide latitude range of isotropic plasma sheet electron precipitation with energies less than 300 keV was observed again. The observations depicted in Figures 1f and 1g exemplify the plasma sheet flux dropout events in this study.

3.2. Correlation With the Large-Scale R1 FAC

On examining plasma sheet flux dropout events measured by ELFIN, we find that the plasma sheet flux dropout events are well correlated with the large-scale R1 field-aligned current (FAC), that is, in most cases in the upward

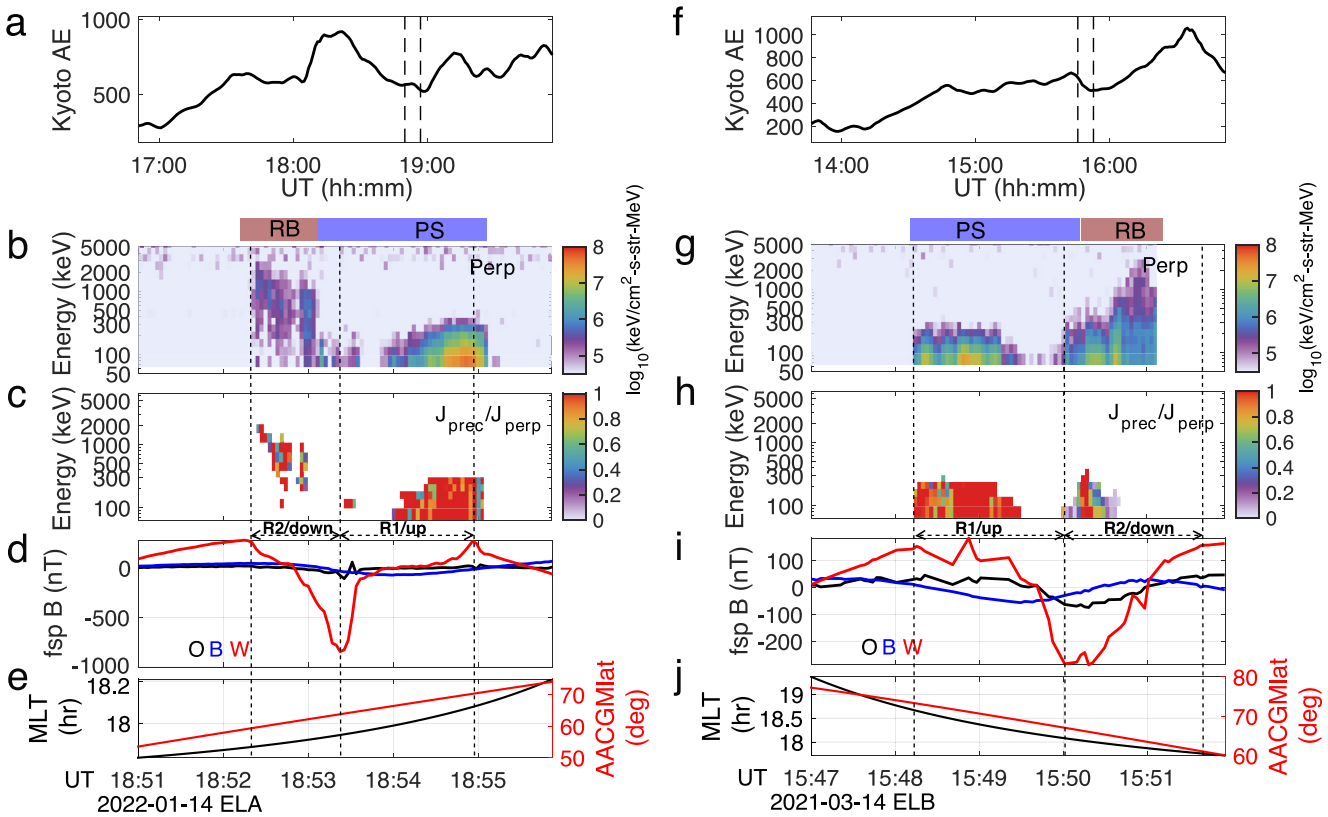

Figure 2. Two examples of plasma sheet electron flux dropouts associated with R1 field-aligned currents near 18:54 UT on 14 Jan 2022 (a–e) and near 15:50 UT on 14 March 2021 (f–j), respectively.

current region in the pre-midnight and dusk region. This correlation was consistently observed in the 28 events that have good FGM magnetic field measurements (these events are collected after March 2021). This correlation is expected because the flux dropouts are within the plasma sheet region, where part of the R1 FAC is known to be connected with cross-tail currents and is likely to be driven by pressure gradients there (Birn et al., 1999; Liu et al., 2021, 2022; Vasyliunas, 1970; Xing et al., 2009). We also note that most flux dropout events are located close to the R1/R2 interface.

Figure 2 presents two examples to demonstrate the close association between flux dropouts and the large-scale R1 FAC region, particularly near the R1/R2 interface. Figures 2a and 2f display the AE variations with average AE greater than 500 nT in both cases. Figures 2b–2d and 2g–2i demonstrate that the radiation belt perpendicular and precipitating fluxes are associated with a R2 downward FAC region, but the isotropic plasma sheet fluxes coincide with a R1 upward FAC region. Right on the poleward edge of the R1/R2 interface and within the R1 current region, energetic electron flux dropouts were evident. Although no clear IB signatures were detected in the two events, the plasma sheet region can be clearly identified by high-latitude isotropic fluxes with an energy limit below 300 keV. In this event, the plasma sheet flux dropout seems to be correlated with an embedded FAC region where the slope of the magnetic field perturbation is steeper than the background as reported by Liu et al. (2021).

Note that the magnetic field perturbations are shown in the local Outward/B-field-aligned/Westward (OBW) coordinates, in which the direction b is taken as the IGRF field direction, the direction o is outward in the plane containing the radius vector from the center of the earth to ELFIN, and the direction w is westward. The FAC polarities are derived from the variations of magnetic field perturbations along the ELFIN trajectories; decreasing (increasing) B_w along a southbound orbital trajectory indicates upward (downward) currents.

3.3. Statistics

In total, we have collected 145 energetic electron flux dropout events from ELFIN at the low-altitude extent of the nightside plasma sheet within MLT of 17–6 hr and during the period from April 2019 to September 2022.

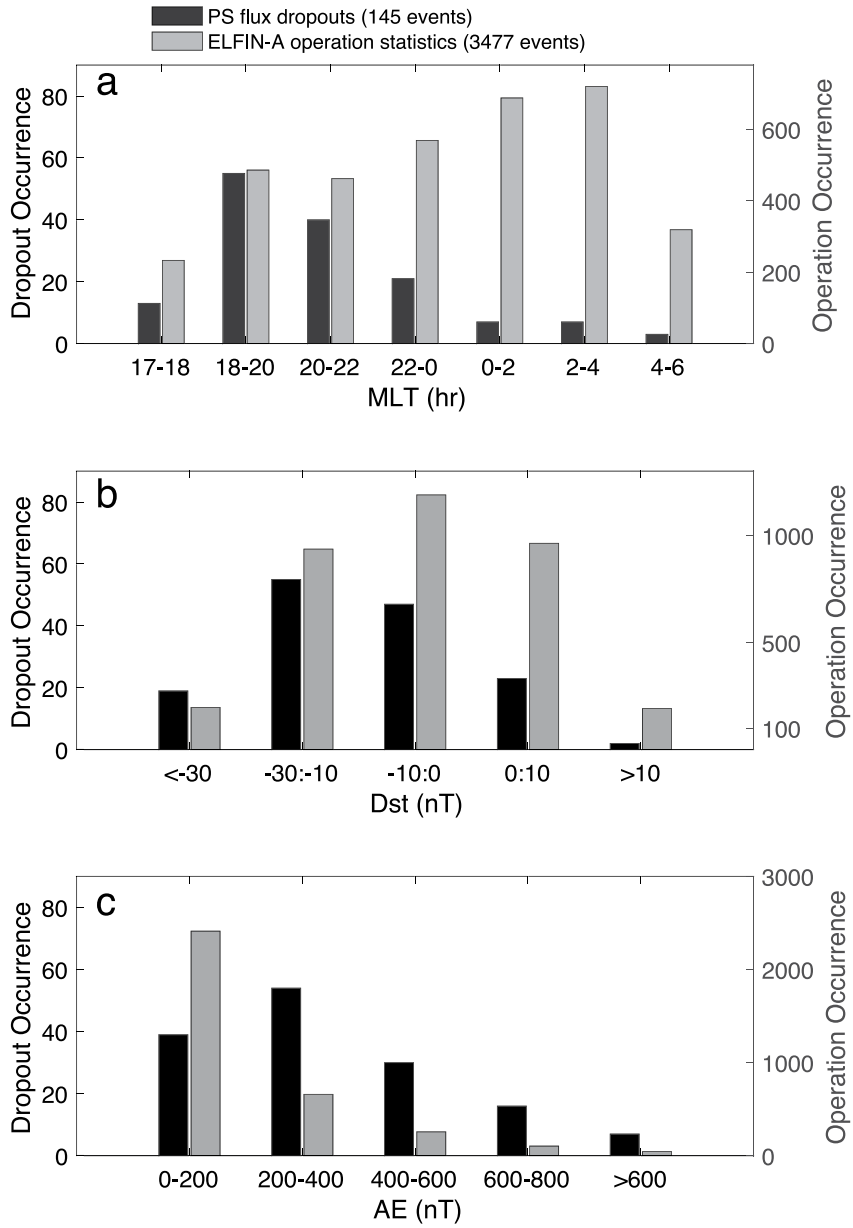

Figure 3. (a) Occurrence distributions of 145 plasma sheet flux dropout events (black) observed by ELFIN-A and ELFIN-B as a function of MLT. The overall ELFIN-A experiments statistical distribution (gray) is also plotted for comparison. (b) Occurrence distributions of dropout events (black) and ELFIN-A operation statistics (gray) in D_{st}. (c) Occurrence distributions of dropout events (black) and ELFIN-A operation statistics (gray) in AE.

Figure 3 displays their occurrence distribution as a function of MLT, D_{st}, AE. To exclude potential bias due to uneven ELFIN residence time, we also show the distribution of ELFIN-A operation statistics within the same MLT range, when good-quality energetic electron measurements are available (as discussed in the data section). Because of small orbital separations of ELFIN-A and ELFIN-B by design, statistics from ELFIN-B is expected to be the same as ELFIN-A's and is thus not shown here.

Figure 3a suggests that the majority of the plasma sheet flux dropout events measured by ELFIN occur in the dusk and premidnight sectors. The scarcity of dropout occurrence in the postmidnight and dawn sectors is in sharp contrast with a preponderance of ELFIN experiments in this MLT range. Thus, the plasma sheet flux dropout events are mainly a phenomenon at dusk and premidnight. Figures 3b and 3c indicate that the flux dropout events seem to also slightly depend on the D_{st} index, in that there is increasing percentage of events occurring

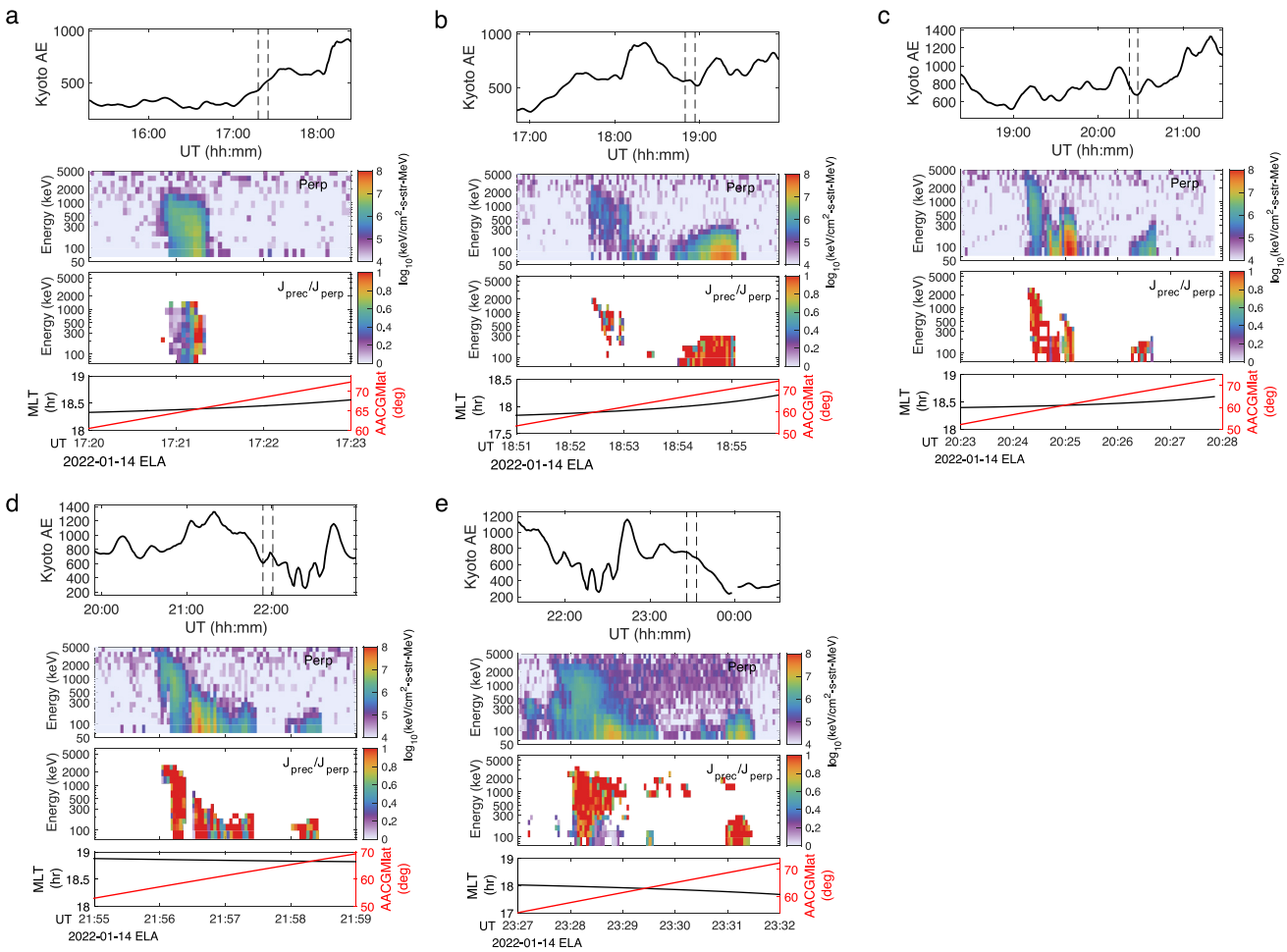

Figure 4. Long-duration plasma sheet flux dropouts observed by ELFIN-A on 14 January 2022. Subfigures a–e show observations near 17:20 UT, 18:55 UT, 20:25 UT, 21:55 UT, and 23:30 UT. For each subfigure of a–e, panels from the top to the bottom are: AE time variations, with the intervals of ELFIN electron measurements indicated by the dashed lines; ELFIN perpendicular electron energy flux spectrogram; ELFIN precipitating-over-trapped electron flux ratios; MLT and magnetic latitude (*Mlat*) in the AACGM coordinates. Note the weak fluxes at 500 keV and above in subfigure e are due to solar energetic particles.

with decreasing D_{st}, albeit the majority of events occur during $D_{st} > -30$ nT. More prominently, they do seem to occur preferentially during substorms or enhanced auroral activities when AE were elevated to more than 200 nT.

We have also examined time duration of some plasma sheet flux dropout events measured by consecutive (≥2) EFLIN orbits when the satellites traversed almost the same spatial location and MLT but at different UT. It seems that flux dropout events can persist several hours, albeit with varying latitudinal widths of flux dropouts. Figure 4 presents one long-duration example observed on 14 Jan 2022 at dusk (MLT ~ 18–19 hr). Flux dropouts did not appear at the beginning a substorm before 17:20 UT (Figure 4a) until the expansion phase and thereafter, lasting for ~5 hr till 23:30 UT (Figures 4b–4e) as the substorm activity gradually subsided.

Based on the SML index (Gjerloev, 2012), we have also interactively identified the correlation between substorm phases, or the phases of enhanced auroral activities, and individual ELFIN flux dropout events. Specifically, if a substorm clearly presents growth, expansion, and recovery phases during an isolated substorm, we categorize the event as related to a specific substorm phase (e.g., Chu et al., 2015; Forsyth et al., 2015; Newell & Gjerloev, 2011). However, when an isolated growth phase or recovery phase cannot be identified, as in the case of multiple auroral activations, we associate the event with either the expansion or recovery phase of enhanced auroral activities. Quiet-time events are characterized by SML > −100 nT. Note that the flux dropout event distributions as a function of SML and time derivatives of $\Delta SML/\Delta t$ have been provided in Supporting Information S1.

With these criteria, we have classified our event distribution as follows: (a) 17 events took place during quiet times, while 128 events happened during substorms or during periods of enhanced auroral activities with

SML < −100 nT; (b) Among the active-time events, 46 events are associated with clearly defined substorms: 6 events align with the growth phase including the onset, 9 events correspond with the expansion phase, and 31 events are tied to the recovery phase; (c) In addition, there are 67 events that are either associated with substorm recovery or occur during the recovery of enhanced auroral activities, and 29 events that are either linked with substorm expansion or occur during the expansion of enhanced auroral activities.

3.4. Potential Magnetospheric Drivers of ELFIN Plasma Sheet Flux Dropouts

Because energetic electrons measured by ELFIN are likely magnetically mapped to the plasma sheet, their absence in ELFIN measurements can potentially be utilized to probe the plasma sheet magnetic field or plasma states associated with substorms. To understand potential magnetospheric driving mechanisms of the flux dropouts at ELFIN altitudes, we next use three conjugate events with magnetospheric spacecraft to study the associated magnetospheric conditions. The conjunction events are between ELFIN, GOES, and THEMIS spacecraft, along with ground-based magnetometer observations and spherical elementary current products to provide context of substorm-related currents.

3.4.1. Event on 2 May 2021

In the first conjunction event, which occurred on 2 May 2021 at dusk with MLT ∼ 18.5 hr, we have ELFIN-A and GOES17 spacecraft observations showing the association of energetic electron flux dropouts with magnetic field B_z decreases near the geostationary equator. Figures 5a and 5b display that the plasma sheet energetic flux dropout event occurred during the substorm expansion phase with AE exceeding 500 nT. Note that the intermittent flux gaps in Figure 5b are due to radio packet drops. Figure 5c indicates that ELFIN-A and GOES17 were in close conjunction with ΔMLT < 1 hr during the time interval of 03:00–03:40 UT, when GOES-17 observed significant B_z decreases and weak B_x increases near the equator at dusk. Such magnetic field variations are consistent with the local current sheet thinning process or twists of field lines due to enhanced perpendicular or azimuthal currents (B_z variations dominate) (Artemyev et al., 2016; Runov et al., 2021). Note that while GOES17 at the equator observed B_z decreases, spacecraft located at high latitudes may well observe B_z increases, because the spacecraft might approach the lobe region during current sheet thinning and magnetic field stretching.

As a result of the magnetic field distortion, as potentially also contributed by R1/R2 FACs at this location, the field lines threading through ELFIN may be projected to the lobe or boundary layer regions, where energetic fluxes above 50 keV are weaker or absent. This interpretation is also consistent with electron energy-latitude dispersion observed near the poleward edge of the flux dropout (Figure 5b), which indicates ELFIN-A was transecting the magnetic footprints of the boundary layer and the central plasma sheet in sequence with increasing latitude (Onsager & Mukai, 1995). The scenario of enhanced current sheets at near-Earth dusk and premidnight is also in agreement with the fact that the flux dropout is usually collocated with an intensified R1 FAC region near the R1/R2 interface, which may close through intensified equatorial azimuthal currents in the same vicinity (Figure 2).

The collocation of the energetic flux dropout measured by ELFIN-A with the R1 FAC region is further shown using spherical elementary current amplitudes (SECAs) analyses based on ground-based magnetometer data (Weygand et al., 2011). Note that we do not have FGM measurements from ELFIN-A for this event. Figure 5e presents the SECA map measured at 03:30 UT in geographic latitude and longitude, representing the FAC distributions concurrent with the plasma sheet flux dropout observed by ELFIN-A. Overlaid on the FAC distribution are the magnetic footprints of ELFIN-A, GOES17, and DMSP spacecraft. The footprints of ELFIN-A at the time of the flux dropout (the magenta thick line) are in close conjunction with the time-averaged (03:00–03:40 UT) footprints of GOES17 in MLT (∼18.5 hr). The footprint of the flux dropout at ELFIN-A was located near $L \sim 10$, and the footprint of GOES17 was at $L \sim 6.6$. Although magnetic mapping is uncertain during substorms, their footprints are near the R1 (bluish downward current regions) and R2 (reddish upward current regions) FAC interface and are mostly within the R1 FAC region. Also, the DMSP F17 data were available for this event and demonstrated that ELFIN observations in the R1 FAC region were well away from the open/closed boundary (near the green thick dot in Figure 5e). This boundary is identified by the equatorward edge of polar rain precipitation and the poleward edge of the large-scale R1 FAC region (e.g., Gallardo-Lacourt et al., 2022; Wing & Zhang, 2015). These DMSP F17 observations have been provided in Figure S1 in Supporting Information S1.

3.4.2. Event on 25 April 2020

For a different scenario, next we present another conjunction event between GOES17 and ELFIN-A at MLT ∼ 21.3 hr, where the plasma sheet flux dropout was observed in close association with the magnetospheric

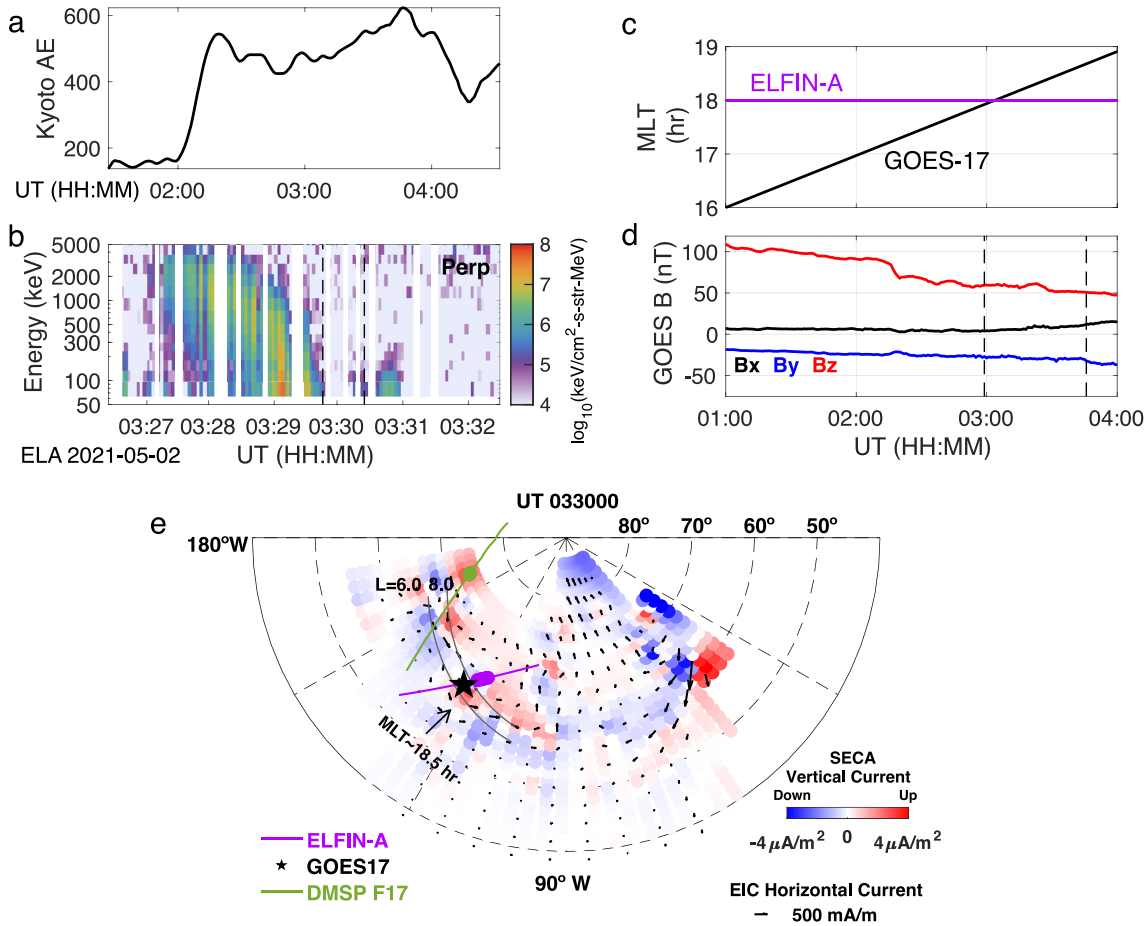

Figure 5. Overview of the conjunction event on 2 May 2021. (a) AE versus universal time (UT). (b) ELFIN-A observations of plasma sheet perpendicular electron flux dropout, as indicated between the dashed lines. (c) ELFIN-A (magenta) and GOES17 (black) MLT as a function of time. (d) Magnetic field measurements by GOES17 at geostationary orbit. The conjunction period with ELFIN-A was indicated between the dashed line. (e) Spherical elementary current amplitudes (SECAs, blue and red) and equivalent ionospheric currents (EICs, arrows) as a function of geographic latitude and longitude. The star symbol indicates the magnetic footprint of GOES17 during the conjugacy period. The magenta line indicates the magnetic footprints of ELFIN-A, with the flux dropout region highlighted in a thicker line. The DMSP F17 magnetic footprints have also been shown here. The magnetic footprints of ELFIN-A (in the southern hemisphere), GOES17 (at magnetospheric equator), and DMSP17 (in the northern hemisphere) have been field-line traced to the northern hemisphere to compare with the SECA map, using the T01 model (Tsyganenko, 2002) with real-time solar wind parameter inputs. The magnetic footprints of $L = 6$ and $L = 8$ have also been shown as the gray solid lines.

dipolarization (B_z increases). Figures 6a and 6b indicates that the plasma sheet flux dropout was measured by ELFIN-A during a recovery phase of multiple auroral activations near 07:03 UT associated with a substorm. This substorm started near 05:30 UT based on AE and SML variations as well as on THEMIS ASI auroral emissions (not shown here). A short moment before near 06:30 UT, GOES17 traversed the ELFIN-A footprints in MLT near the premidnight sector. The footprint of the flux dropout at ELFIN-A was located near $L \sim 10$, and the footprint of GOES17 was at $L \sim 6.6$. At this time, GOES17 revealed pronounced magnetic field B_z enhancements from ~70 nT to near ~85 nT. Note that the geosynchronous GOES-17 spacecraft traversed a wide range of MLT sectors, spanning from 20 to 23 hr within a 3-hr period, whereas the ELFIN-A observations were solely made near 21 hr MLT.

The observations from GOES-17, which indicate an increase in B_z, suggest the development of magnetic dipolarization extended to the geosynchronous orbit. It is probable that the dipolarization is occurring near the same MLT just beyond the geostationary orbit ($L \sim 10$), which is approximately the location where the ELFIN flux dropout was projected to. In reverse, the absence of B_z increases at geosynchronous orbit does not necessarily negate the potential for B_z increases at larger L-shells in the nightside transition region (Gabrielse et al., 2019; Liu et al., 2016; Sergeev, Chernyaev, et al., 2012). The observed decrease in B_z after 06:30 UT is likely attributable to combined effects of MLT-localization and temporal evolution (a recovery since 06:20 UT) of dipolarization regions near the geosynchronous orbit during the substorm.

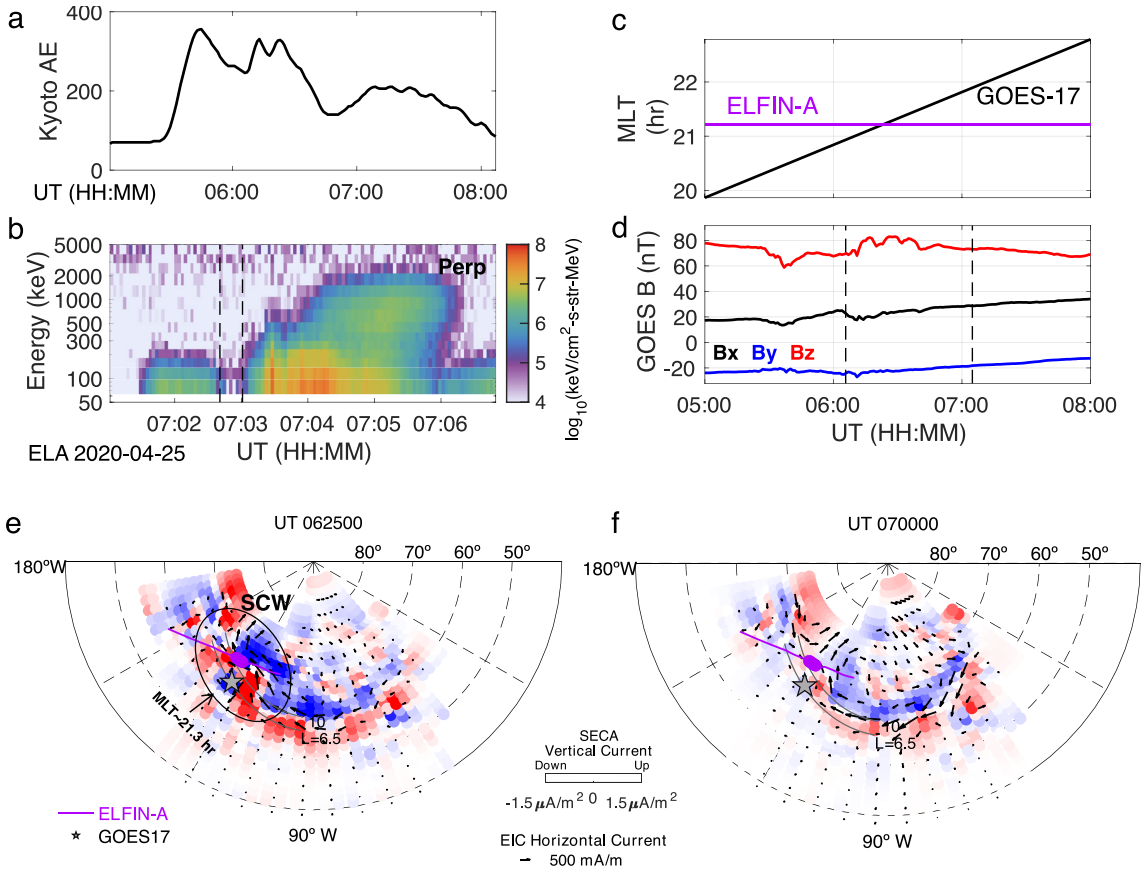

Figure 6. Overview of ELFIN-A and GOES17 conjugate observations on 25 April 2020, presented in the same format as Figure 5. In panel (e), the magnetic footprints of ELFIN-A (magenta line) and GOES17 during the conjugacy period (star symbol) are within the substorm current wedge (SCW) system near MLT ~ 21.3 hr in the premidnight sector. The thicker magenta line indicates the location of the ELFIN-observed flux dropout. The magnetic footprints of ELFIN-A (in the southern hemisphere) and GOES17 (near the magnetospheric equator) have been field-line traced to the northern hemisphere to compare with the SECA map. The approximate region of strong SCWs has been indicated by the black oval. The SCW can be identified by eye through a pair of upward (reddish vertical currents) and downward (bluish vertical currents) FAC regions between which strong westward EICs flow. Individual ground-based magnetometer data have been examined to verify ΔH and ΔD variations within the SCW region and at mid-latitudes (not shown here). Panel (f) displays the SECA map measured near 07:00 UT when the flux dropout was observed by ELFIN.

Such dynamic evolution of the magnetospheric dipolarization may be remotely sensed via observations from the ground-based magnetometers. Figure 6e displays the SECA map and the magnetic footprints of ELFIN-A and GOES17 near 06:25 UT, presented in the same format as Figure 5e. The flux dropout observed by ELFIN-A was observed located near the interface of high-latitude upward (red data points) and downward (blue data points) current region, collocated with the strong westward electroject represented by EIC horizontal currents. The magnetic footprint of GOES17 was located slightly equatorward and at the interface of another pair of downward/upward currents, of which the polarities reversed compared with their high-latitude counterparts. These features are consistent with the substorm current wedge (SCW). The ground-based magnetometers within the SCW (not shown here) confirmed that ΔD is positive east of the ELFIN-A flux dropout and negative west of it.

The mid-latitude stations also verified that ΔH variations are positive at equatorward, indicating the magnetospheric dipolarization. The magnetic observations from five mid-latitude stations, together with their relative positions to the GOES and ELFIN footprints, have been provided in the Supporting Information S1 section. In particular, the positive ΔH perturbations revealed that the elevated magnetospheric magnetic fields or the dipolarizaton persisted until ~07:00 UT when ELFIN observed the energetic electron flux dropout near the end of the substorm recovery phase. Similarly, we note that the SECA map measured at 07:00 UT and the FAC patterns and locations relative to the ELFIN flux dropout shown in Figure 6f resemble those measured at 06:25 UT in Figure 6e, but the measurements at 07:00 UT exhibit smaller current amplitudes. Although there exists a time lag of near 30 min between the activation of the magnetic dipolarization and the observed flux dropout by ELFIN, the

ground-based and in-situ observations provide evidence that the plasma sheet flux dropout was likely associated with the large-scale magnetospheric dipolarization process.

It is noted that the typical timescales for both the buildup of the substorm current wedge and the manifestation of enhanced currents are usually less than half an hour. However, the global magnetic field dipolarization associated with substorms or increased auroral activities exhibits a different timescale. This can last several hours or more, particularly during consecutive activations. The dissipation of magnetic field enhancements is mainly determined by ionospheric resistivity, and can persist throughout the recovery phase (e.g., Kepko et al., 2014, 2015). The global dipolarization will also expand azimuthally and tailward (e.g., Gabrielse et al., 2019), and the B_z increase associated with global dipolarization can be sustained a long period in the same region with the timescales comparable with the entire substorm, which is usually 3–4 hr (e.g., Tanskanen et al., 2002). These timescales align with our statistical result that the flux dropout was observed in all phases of substorms and is more frequently observed during the substorm recovery phase or during the recovery of enhanced auroral activities.

Although no observations are available to reveal the associated energetic electron distributions near the magnetospheric equator that are linked to ELFIN measurements, we expect that the strong magnetic field B_z increase will probably be associated with highly perpendicularly anisotropic energetic electrons in the near-Earth magnetotail due to betatron acceleration (Birn et al., 2014; Smets et al., 1999; Turner et al., 2016; Ukhorskiy et al., 2022). Because the loss cone of energetic electrons in the near-Earth tail is only a few degrees, no significant energetic electron fluxes will be adiabatically projected to the ELFIN altitude if most electrons are depleted at low pitch angles and have only perpendicular pitch angles. Thus, the expected electron perpendicular anisotropy in this event is likely associated with magnetic dipolarizations, possibly explaining the plasma sheet dropout observed by ELFIN-A.

3.4.3. Event on 7 September 2022

To further illustrate the potential link between electron perpendicular anisotropy in the near-Earth magnetosphere and plasma sheet flux dropouts at ELFIN, next we examine another event when the THEMIS and ELFIN-B observations were in nearby MLT (ΔMLT $\sim$ 1.5 hr). Figure 7 depicts an overview of ELFIN-B energetic electrons, ions, and the associated magnetic perturbations measured near 19:15 UT on 07 September 2022 in the premidnight (MLT $\sim$ 22.5 hr) auroral region during the recovery phase of a substorm (Figures 7a and 7f). The energetic electron flux dropout was observed within the isotropic flux region of the plasma sheet. The plasma sheet electrons are identified by assuming an upper energy limit of $\sim$300 keV and were observed poleward of the relativistic (>1 MeV) electron fluxes in the outer radiation belt (Figures 7b and 7c). The electron isotropy boundary (IB) signature is unclear in this case.

ELFIN also obtained energetic ions in this event, which reveal an ion isotropy boundary well within the electron outer radiation belt (Figures 7d and 7e). Because significant perpendicular energetic ions have been observed to be associated with the flux dropout (Figure 7d), it is unlikely that the energetic electron dropout is explained by magnetic field line distortions and the projection of field lines connecting ELFIN to the lobe. In addition, the magnetic field measurements for this event are still under calibration, thus we currently do not have a direct observation of FACs associated with the plasma sheet flux dropout in this case. However, because the flux dropout occurred poleward of the IB and within the isotropic flux of the electron plasma sheet region, we expect the flux dropout to be associated with the R1 FAC region (similar to those shown in Figure 2).

Coinciding with ELFIN-B measured flux dropouts, THEMIS-D was located close to the magnetospheric equator at $\sim$12 R_E in the midnight sector of MLT $\sim$ 0 hr Figure 8 shows that THEMIS-D observed prolonged energetic injection electrons from 18:00 UT to $\sim$19:40 UT, which were accompanied by sporadic dipolarizing flux bundles (DFBs) with magnetic field B_z increases and earthward bursty bulk flows (BBFs) (Angelopoulos et al., 1993; Liu et al., 2013). Both perpendicular and parallel anisotropy of energetic (>30 keV) electron fluxes were observed during this period (Figure 8g). A rather strong example of DFB and BBF was measured by THEMIS-D near the equator (Figures 8b–8e) only less than 20 min before ELFIN-B observed the plasma sheet flux dropout (Figure 7). Note that the flux depletion measured by THEMIS-D when ELFIN-B measurements were taken is a result of THEMIS-D's entry into the plasma sheet boundary layer, as evidenced by a sudden increase in B_x/B_{lobe}. This flux depletion is not directly linked to plasma sheet flux dropouts observed by ELFIN-B.

We also acknowledge that energetic electrons associated with small-scale BBF/DFBs observed by THEMIS-D at $\sim$12 R_E cannot be directly linked to the flux dropout observed by ELFIN-B in Figure 7 due to electron drift effects.

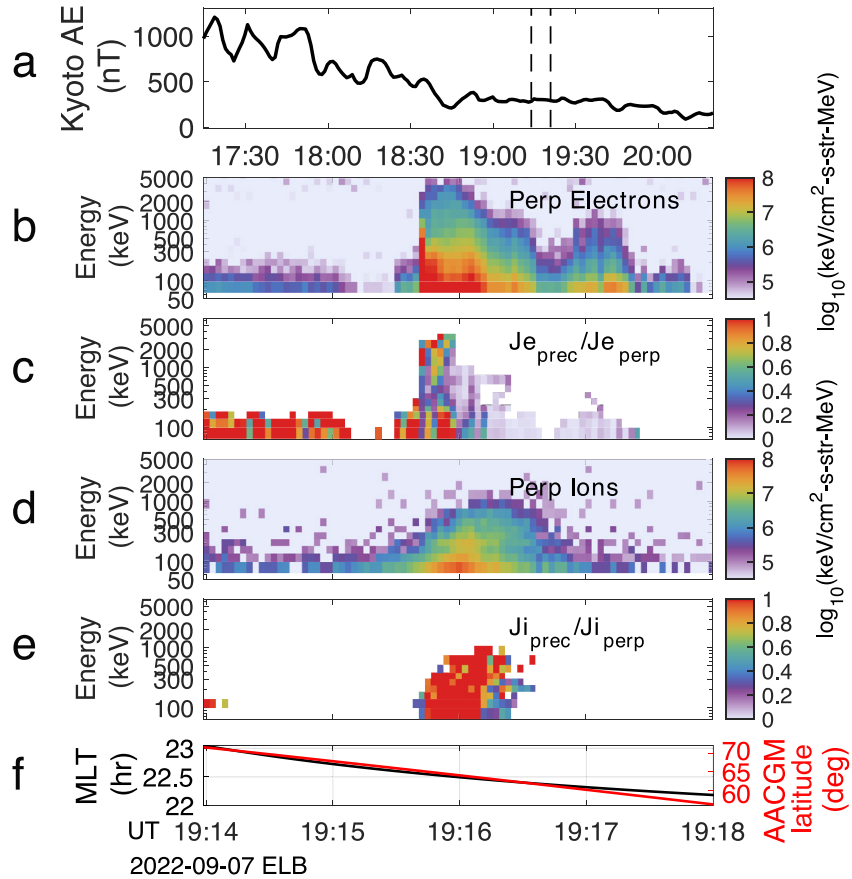

Figure 7. Summary of ELFIN-B observations on 07 September 2022. (a) AE versus UT. (b) Perpendicular electron flux energy-time spectrogram. (c) Electron precipitating-over-perpendicular flux ratios. Je_{prec} and Je_{perp} represent the electron precipitating and perpendicular fluxes, respectively. (d) Perpendicular ion flux energy-time spectrogram. (e) Ion precipitating-over-perpendicular flux ratios. Ji_{prec} and Ji_{perp} represent the ion precipitating and perpendicular fluxes, respectively. (f) Time variations of MLT and magnetic latitude (*Mlat*) in the AACGM coordinates.

Instead, we assume that the global-scale dipolarization closer to the Earth ($L \sim 7$–12) may be the cause of the perpendicular anisotropy and energetic flux dropout at ELFIN, though there were no ground-based magnetometer data available to verify this speculation. The small-scale BBF/DFBs likely provide a source of energetic electrons associated with the flux dropout closer to the Earth and near the edge of the outer radiation belt (Birn et al., 2019; Merkin et al., 2019). This source processes have been shown by previous studies (e.g., Birn et al., 2013; Gabrielse et al., 2017; H. Fu et al., 2020), which demonstrated that the sharp gradients in the magnetic field DFB can trap electrons as electrons drift around the Bz peak. The trapped energetic electrons will travel toward the Earth along with the DFB field if the DFB remains sufficiently larger than the background magnetic field. The perpendicular anisotropy and parallel flux depletion are likely generated by betatron acceleration processes associated with magnetic field B_z elevation (e.g., Birn et al., 1999; Turner et al., 2016; Ukhorskiy et al., 2022).

We also note that THEMIS and ELFIN observations were separated by 1.5 hr in MLT, and that energetic electrons will gradient- and curvature drift eastward from the THEMIS position. However, our assumption is that the azimuthal extent of flux dropouts may align with the spatial scale of global dipolarization or multiple BBF/DFBs that spread over a wide azimuthal extent. These can extend up to 5 hr in MLT in the region near Earth during substorm events (e.g., Gabrielse et al., 2019; Gkioulidou et al., 2015; Wiltberger et al., 2015).

To support our expectation for the formation of perpendicular anisotropy and parallel flux depletion, we will use the Liouville mapping technique to model the evolution of electron distributions measured at THEMIS-D associated with earthward BBFs and DFBs (the gray-shaded region in Figure 8), as magnetic field lines undergo topological changes during dipolarization (e.g., Apatenkov et al., 2007; Mauk & Meng, 1987). We assume the initial state of the magnetic field does not deviate much from the empirical Tsyganenko model. Therefore, we

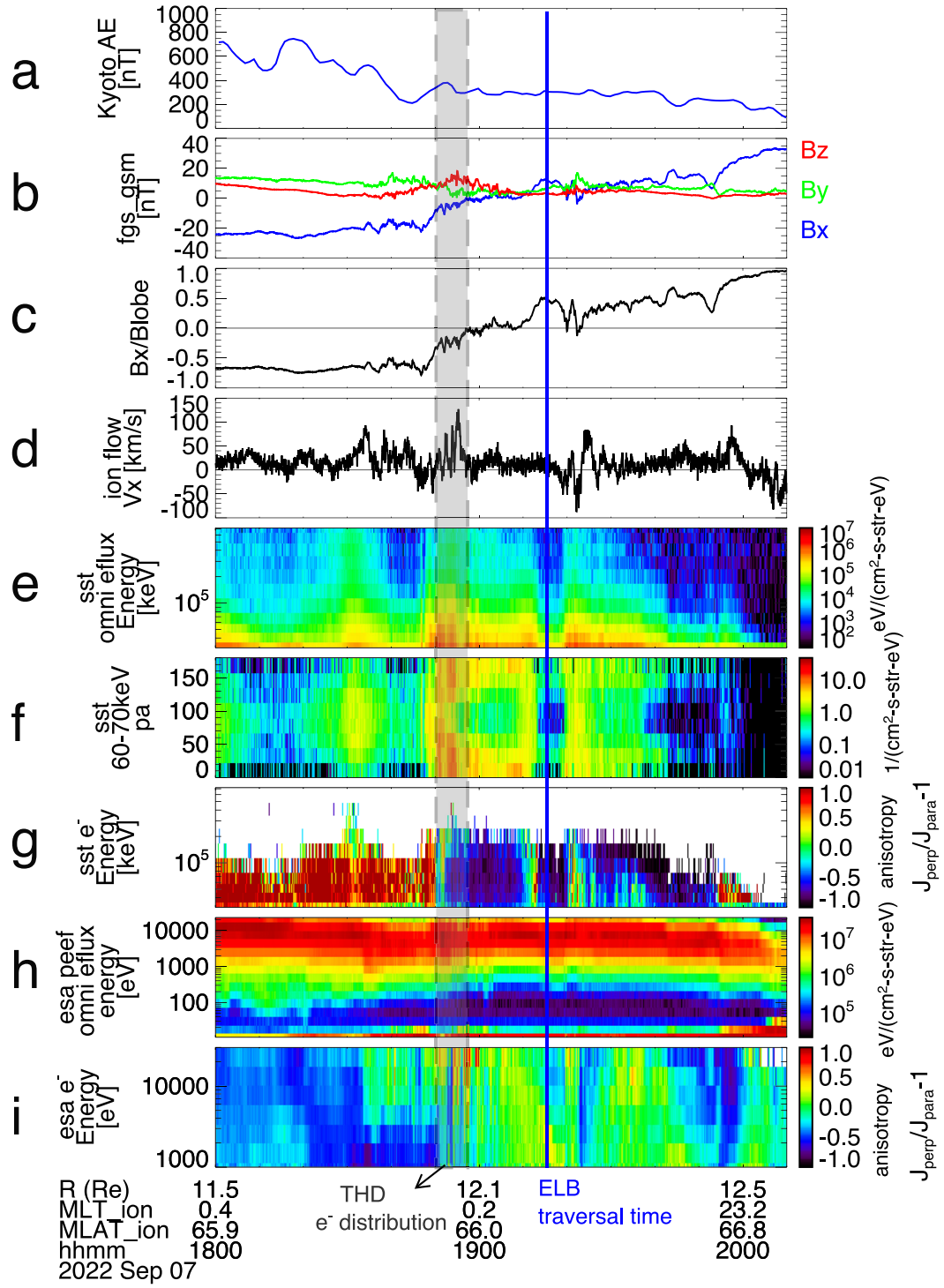

Figure 8. Summary of THEMIS-D observations in the equatorial magnetosphere during the conjunction event with ELFIN-B on 07 September 2022. (a) AE. (b) Spin-resolution (~3 s) vector magnetic fields in the GSM coordinates. (c) B_x/B_{lobe} where $B_{lobe} = \sqrt{2\mu_0 P_{tot}}$ and P_{tot} is the total pressure containing only B_x and B_y components (e.g., Liu et al., 2013). (d) Ion bulk flow velocity V_x. (e) Omni-directional energy fluxes for electrons >30 keV measured by SST. (f) Pitch-angle spectrogram of 60–70 keV electrons measured by SST. (g) Electron flux anisotropy J_{perp}/J_{para}-1 measured by SST, where J_{perp} is electron fluxes measured within the pitch angle range of 75°–105°, and J_{para} is the larger of the electron fluxes measured within the pitch angle ranges of 0°–30° and 150°–180°. (h) Omni-directional energy fluxes for electrons <25 keV measured by ESA. (i) Electron flux anisotropy calculated in the same format as (g). The blue vertical line indicates the time stamp when ELFIN-B measured plasma sheet flux dropout.

trace out the entire field line using the T01 model from the THEMIS-D location with inputs from real-time solar wind parameters. The equatorial point of resultant magnetic field line is considered as the starting point for the electron distribution. We then assume that a final state of the dipolarized magnetic field can be represented by the IGRF field, with an equatorial point at ~8 R_E as BBFs propagate inward along with the injected electrons. We select $L = 8$ primarily based on the locations of flux dropouts observed by ELFIN-B in Figure 7. This choice is also informed by numerous other instances where flux dropout events have been observed just outside the outer edge of the radiation belt. Particularly in the case illustrated in Figure 7, the flux dropout region was mapped to the magnetospheric equator within $L \sim 6$–7 using the IGRF model, and within $L \sim 8$–14 using the T01 model. It is important to note that magnetic field mapping during substorm events may have large uncertainties, potentially spanning several Re in radial equatorial distance. Thus, for a qualitative demonstration of how perpendicular anisotropy may form in the near-Earth region, we selected $L = 8$ as a representative value for our simulation.

This model setup is intended for a rough illustration of the field line contracting and dipolarizing processes during a substorm and is not intended for comparison with realistic electron distributions in the magnetosphere as pertinent to ELFIN-B observations in the ionosphere. Figure 9a demonstrates the magnetic field models in the GSM $X - Z$ plane we use for Liouville mapping of electron distributions. Figure 9c displays the electron energy and PAD from THEMIS-D observations, which will be used as the initial electron distribution at the equator of the initial field line (the blue curve in Figure 9a). The electron flux distribution has been normalized so that $\iint f_{\mathrm{norm}}(\alpha, E)\, d\alpha\, dE = 1$.

For Liouville phase-space mapping, we assume conserved first and second adiabatic invariants, that is, both plasma wave scattering and field-line curvature scattering effects have been neglected here (Artemyev, Angelopoulos, et al., 2022; Artemyev, Neishtadt, et al., 2022; Sergeev et al., 1983; Shen et al., 2022). We then have the following relation:

$$\mu = \frac{E\sin^2\alpha_{eq}}{B(0,t)} = const$$
$$\int_{l_1}^{l_2} \sqrt{E - \mu B(s,t)}\, ds = \sqrt{E}\int_{l_1}^{l_2} \sqrt{1 - \sin^2\alpha_{eq}\frac{B(s,t)}{B(0,t)}}\, ds = const \quad (1)$$

where E is the electron energy, α_{eq} is the pitch angle at the equator, μ is the first adiabatic invariant, $B(s, t)$ is the magnetic field intensity along the field line s with $B(0, t)$ representing the value at the equator, and l_1 and l_2 are the magnetic mirror latitudes in the northern and southern hemisphere, respectively. Then, we can numerically solve the electron energy and pitch angle at any location, given an initial energy and PAD (Figure 9c) and configurations of magnetic field lines (Figure 9a).

Figure 9d presents the mapped electron distribution at the equator of the dipolarized IGRF magnetic field in Figure 9a. Most electrons near the loss cone are energized by tens of keV, but perpendicular electrons are accelerated to more than 100 keV due to the magnetic field increase during the dipolarization and earthward propagation. Because of the predominant betatron acceleration associated with this dipolarization process, electron fluxes are depleted near the loss cone and develop a broad maximum at perpendicular pitch angles. Figures 9e and 9f further illustrate the evolution of electrons in energy and pitch angle due to the dipolarization, and reveal that electrons are mostly betatron accelerated in the perpendicular direction (solid red lines). The electrons experience only weak Fermi-type parallel acceleration (the solid blue line in Figure 9e). These perpendicularly anisotropic energetic electrons will not be captured by a low-altitude spacecraft and will likely appear as energetic electron flux dropouts as observed by ELFIN.

It is worth discussing here whether the large perpendicular anisotropy of energetic electrons in Figure 9 can last for a sufficiently extended period in the near-Earth region, in order to explain the plasma sheet flux dropout events measured by ELFIN. Typically, the perpendicular electron anisotropy and depleted loss-cone fluxes will self-consistently destabilize whistler-mode waves or electron cyclotron harmonic (ECH) waves, both of which may effectively scatter and precipitate <50 keV electrons from the plasma sheet (e.g., Ni et al., 2016), thus limiting the level of modeled perpendicular anisotropy (Kennel & Petschek, 1966). However, the efficiency of whistler- or ECH-scattering falls off rapidly with increasing energy beyond 50 keV in the plasma sheet, and the associated lifetime of energetic (>50 keV) electrons is expected to be at least several hours (Ni, Thorne, Meredith, et al., 2011). Also, field-line curvature scattering is likely not significant during dipolarization when the magnetic

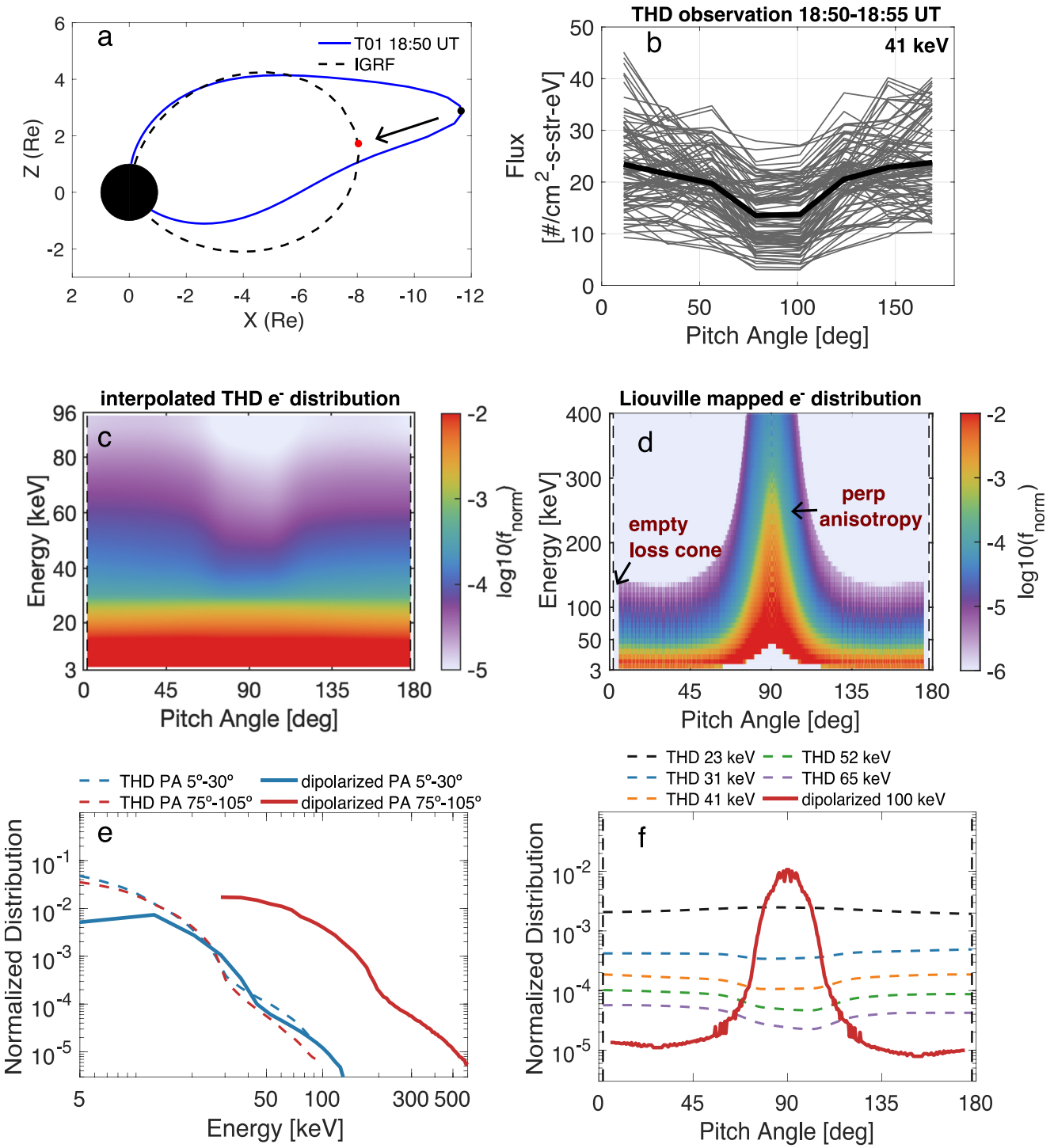

Figure 9. (a) Magnetic field configurations in the GSM $X-Z$ plane of field lines before dipolarization takes place with an equatorial point (black) at ~$12R_E$ and after dipolarization with an equatorial point (red) at ~$8\ R_E$. (b) An example of measured electron pitch-angle distributions (PADs) at 41 keV by THEMIS-D within the DFB and BBF region, as highlighted by gray-shading in Figure 8. (c) THEMIS-D measured electron energy and PAD, which is interpolated with finer energy and pitch angle grids. (d) Liouville mapped electron distribution at the equator of the dipolarized magnetic field. Note that the depleted electron fluxes below 50 keV at perpendicular pitch angles are artificial, caused by the energy cutoff of the initial distribution at below 3 keV. (e) Electron energy distributions at parallel (blue, 5°–30°) and perpendicular (red, 75°–105°) pitch angles before (dashed lines) and after (solid lines) the magnetic field dipolarization. (f) Electron PADs at several different energies before (dashed lines) and after (red solid line) acceleration due to the magnetic field dipolarization.

field line curvature radius increases (Lukin et al., 2021), especially for electrons at high pitch angles (Buchner & Zelenyi, 1989; Delcourt et al., 1995). The kinetic Alfvén wave has recently been found to potentially contribute to the precipitation of >50 keV electrons from the substorm plasma sheet, but this scattering is most effective when KAW power is strong enough (Shen et al., 2022, 2023), which is not always observed. Furthermore, the perpendicular anisotropy will be continuously fed by freshly injected electrons during a substorm, thus its lifetime is expected to be consistent with substorm timescales. Based on these considerations, it is plausible to assume that the energetic electron perpendicular anisotropy will be able to sustain a prolonged period to account for the plasma sheet flux dropout signatures observed by ELFIN.

4. Discussion

Although many prior investigations of energetic electron flux dropouts have been focused on relativistic electrons from the outer radiation belts (e.g., Bortnik et al., 2006; Morley et al., 2010; Onsager et al., 2002; Shprits et al., 2006; Turner et al., 2012; Xiang et al., 2017), only a handful of studies have reported energetic electron flux dropouts from the plasma sheet region (Baker & McPherron, 1990; Bogott & Mozer, 1973; Fennell et al., 1996; Huang et al., 2003; Moldwin et al., 1995; Sauvaud & Winckler, 1980). No such dropout events have been previously reported in the low-altitude projection of the plasma sheet, mainly due to a lack of energetic electron measurements with sufficiently wide ranges of energy and pitch-angle coverage. Energetic particle observations from low-altitude spacecraft provide a unique perspective, through which it is possible to remotely probe, almost instantaneously, a wide range of latitudinal/L-shell regions in the magnetosphere. This global or regional characterization of magnetospheric magnetic field and plasma states is otherwise challenging to attain using sparse magnetospheric satellite observations, yet is critical to model substorm plasma sheet magnetic configurations.

Fennell et al. (1996) utilized statistical measurements of energetic electron flux dropouts from CRRES and found that the dropout events were primarily in the dusk and premidnight sectors within the L-shell range of ∼7–9 and at magnetic latitudes of >10°. While left unexamined for their AE dependency, their events were predominantly observed during moderate to high geomagnetic activities as indicated by the K_p index. Also, the majority of their events were associated with low or modest D_{st} variations, thus exhibiting no dependence on magnetic storms. These statistical patterns of occurrences are in surprising agreement with ELFIN observations in the ionosphere (Figure 3). Because ∼20% of their events had both proton and electron dropouts associated with local magnetic field increases and strong cross-tail currents, they suggested that these events were consistent with the satellite approaching and crossing a R1 current system and exiting to the plasma sheet boundary layer or lobes. Therefore, the observations and conclusions reached by Fennell et al. (1996) are in good agreement with the first type of our plasma sheet flux dropout events observed by ELFIN (as demonstrated in Figure 5).

Many of our flux dropout events may fall into this first type, where the local enhancements of cross-tail current sheets (thinning as well) and R1 FACs cause significant magnetic field distortions around their local neighborhood (Ganushkina et al., 2010), and the field lines that thread through the low-altitude ELFIN in the ionosphere are likely twisted toward the boundary layer or lobe regions where energetic fluxes above 50 keV are weaker or absent. It is well-known that the R1/R2 FACs during substorms are amplified by more than twofold (Iijima & Potemra, 1978; Yang et al., 2012), typically associated with the plasma pressure buildup in the near-Earth (L ∼ 6–15) substorm plasma sheet (Artemyev et al., 2019; Birn et al., 1999; Shiokawa et al., 1998; Vasyliunas, 1970; Yang et al., 2012). The pressure buildup has a slight preference toward the dusk and premidnight sectors (Gkioulidou et al., 2009; Merkin et al., 2019), consistent with the premidnight prevalence of bursty-bulk flows (BBFs), flow-braking, and particle injections that lead to the pressure buildup (Angelopoulos et al., 1994; Ergun et al., 2015; Gabrielse et al., 2019; Liu et al., 2016). Thus, magnetic field distortions by enhanced tail currents and R1/R2 FACs during substorms are likely more prominent in the dusk and premidnight sectors.

The second type of ELFIN plasma sheet flux dropout events is likely produced by magnetospheric electron perpendicular anisotropy as a result of betatron acceleration associated with global magnetospheric dipolarizations(Birn & Hesse, 2013; Turner et al., 2016). The formation of the perpendicular anisotropy due to betatron acceleration is often associated with electron depletion at low pitch angles (Figure 9d), so that most electrons cannot reach ELFIN at low altitudes before mirroring back toward the equator. Examples of this type of flux dropout and the generation of the energetic electron perpendicular anisotropy during substorm dipolarizations have been shown in Figures 6–9. Because the magnetic field dipolarization is typically observed around the

center meridian of the SCW (e.g., Kepko et al., 2014; McPherron et al., 1973; Yang et al., 2012), this subset of dropout events is more likely to occur near the premidnight sectors than at dusk. It is worth noting that the majority (~80%) of the events reported by Fennell et al. (1996) in the plasma sheet have no simultaneous proton and electron flux dropouts. It is thus likely that some mechanism other than just the spacecraft entry into the lobes was at play in these events. One possibility may be the plasma anisotropic distributions associated with magnetospheric reconfigurations.

The perpendicular anisotropy and parallel flux depletion, triggered by field dipolarizations and contractions, only represent one likely source mechanism. It is not necessarily the sole mechanism leading to the dropouts associated with global dipolarizations. For example, the shift in electron gradient and curvature drift paths around dipolarization field enhancements, and the change in the corresponding Alfvén layer, should also be considered. Specifically, the studies by Gabrielse et al. (2017, 2019) have demonstrated that the Alfven layers for energetic electrons undergo significant modifications during global dipolarization processes. Energetic electrons are likely to drift around the dipolarized field enhancement, and will be deflected tailward on the duskside and earthward on the dawnside due to the spatial distribution of magnetic field gradients around the dipolarization. Additionally, a depletion of energetic electrons is also likely near the duskside magnetic field gradients. These nonlocal effects of Alfvén layer modifications cannot be resolved by our localized observations. A more systematic approach is required, such as combining test particle simulations with global MHD fields (e.g., Birn et al., 2013, 2019; Eshetu et al., 2019; Merkin et al., 2019; Wiltberger et al., 2015).

Furthermore, we note that magnetic dipolarizations in the plasma sheet may not be a sufficient condition to produce perpendicular anisotropy and flux dropouts, because electrons may be scattered by the magnetic field line curvature in the midtail plasma sheet where the local magnetic field is weak (e.g., Eshetu et al., 2018, 2019). Thus, in our events flux dropouts were not observed in the midtail plasma sheet associated with dipolarizations but only in the near-Earth region where B_z is sufficiently strong to prevent fast curvature-induced pitch-angle scattering.

In addition, the ELFIN measurements are limited to specific times and MLT locations during the two conjunction events (Figures 6 and 7), and it is likely that the energetic electron flux dropout may indeed occur after the dipolarization with substantial time lags (e.g., on the order of ~30 min). The observations available in our study cannot exclude the possibility that, even when the dipolarization serves to provide a source electron population with perpendicular anisotropy, the energetic electron flux dropout may later occur in a different region with a considerable time delay. Thus, some other processes such as the energy and pitch-angle dependent electron drifts might be at play in converting the electrons injected from the dipolarization region into a source of the energetic electron flux dropout. The detailed mechanisms including electron drift effects need to be examined for better understanding and modeling of the energetic electron flux dropout in the future.

To rigorously pinpoint the physical processe responsible for plasma sheet flux dropouts observed by ELFIN at low altitudes requires simultaneous energetic electron and ion flux and pitch-angle measurements at ELFIN, as well as magnetic fields and energetic electron distributions at magnetospheric satellites that are linked to the ionospheric observations. These requirements are barely satisfied for the majority of our observations. We are thus currently unable to draw a definitive conclusion on the mechanisms that lead to flux dropout events in most individual cases.

We also emphasize that the EFLIN plasma sheet flux dropout events have perpendicular fluxes almost completely disappearing during substorms. Thus, our events are distinct from the plasma sheet precipitating flux decreases, or the precipitating-over-trapped flux ratio dropoffs, associated with B_z enhancements during long-duration steady magnetospheric convection (SMC) as shown by Sergeev et al. (2018). Because the time duration of ELFIN flux dropout events is typically tens of minutes or longer, comparable with the substorm time scales, our observations are also different from injection electron drifting holes that have duration of only 1–2 min at geosynchronous orbit (Sergeev et al., 1992).

5. Conclusions

Using ~3.5 years of measurements of energetic (>50 keV) electron distributions from the ELFIN CubeSats in the high-latitude ionosphere, we have reported, for the first time, statistical distributions of energetic electron flux

dropouts in the ionospheric projection of the plasma sheet. We observed a total of 145 such energetic electron flux dropout events within the MLT range of 17–6 hr, and identified several key characteristics, including:

- The majority of the plasma sheet flux dropout events measured by ELFIN occur in the dusk and premidnight sectors.
- Flux dropouts occur preferentially during substorms and enhanced auroral activities when AE is elevated to more than 200 nT and when SML is less than −100 nT.
- Flux dropouts are also well correlated with the R1 FAC region and often are located near the interface between R1 and R2 FAC regions.
- Flux dropouts can persist for tens of minutes to hours, comparable with substorm time scales.

To better understand the potential magnetospheric drivers and magnetic field conditions that lead to plasma sheet flux dropouts at ELFIN altitudes, we studied three conjunction events using data from ELFIN, GOES, and THEMIS spacecraft. Our analyses were supplemented by ground-based magnetometer observations and spherical elementary current products. Our findings suggest that one type of plasma sheet flux dropouts may be linked to local enhancements and thinning of cross-tail current sheets (Artemyev et al., 2016; McPherron, 1972; Runov et al., 2021), as well as amplified R1 FACs (Yang et al., 2012). These intensified currents cause significant magnetic field distortions around their local neighborhood (Ganushkina et al., 2010), and the field lines that thread through the low-altitude ELFIN in the ionosphere are likely twisted toward the boundary layer or lobe regions, where energetic fluxes above 50 keV are weaker or absent. The majority of our events occurred at dusk and likely fall into this category. Indeed, enhancements and thinning of magnetotail current sheets have been observed to form more likely on the duskside than the dawnside. This dawn-dusk asymmetry has been demonstrated through both statistical observations and self-consistent numerical simulations (e.g., Lu et al., 2018). The other type of plasma sheet flux dropout may be caused by magnetospheric electron perpendicular anisotropy, resulting from predominant betatron acceleration associated with magnetic field B_z increases and magnetic dipolarizations near premidnight (Kepko et al., 2014; Turner et al., 2016). It is also likely that the shift in electron gradient and curvature drift paths around dipolarization field enhancements and the change in the corresponding Alfvén layer contribute to the flux dropouts.

Understanding the variability of energetic electron fluxes in the plasma sheet region are particularly important for probing instantaneous and local magnetospheric magnetic field and plasma states during substorms. The two types of plasma sheet flux dropouts discussed here are linked to specific, albeit not fully defined, magnetic field configurations during substorms at particular magnetic local times. Consequently, the particle signatures of plasma sheet flux dropouts at ELFIN could serve as a valuable tool for gauging and refining magnetic field models, along with other signatures such as the isotropy boundary (Dubyagin et al., 2002; Sergeev et al., 1993). This, in turn, could improve the accuracy of field-line mapping during substorms.

Data Availability Statement

ELFIN data can be publicly accessed from https://data.elfin.ucla.edu/. The flux dropout event list can be accessed through https://doi.org/10.5281/zenodo.8136713 (Shen, 2023). THEMIS spacecraft and ground-based data are avaliable at http://themis.ssl.berkeley.edu. GOES data are obtained from https://www.ngdc.noaa.gov/stp/satellite/goes/. DMSP data products can be accessed from https://satdat.ngdc.noaa.gov/dmsp/data/ and http://sd-www.jhuapl.edu/Aurora/. EICs and SECAs data sets can be accessed from https://doi.org/10.21978/P8D62B (Weygand, 2009a) and https://doi.org/10.21978/P8PP8X (Weygand, 2009b). Data access and processing was done using SPEDAS V3.1, see Angelopoulos et al. (2019). The SML index is readily available from the SuperMAG website https://supermag.jhuapl.edu and the AE index is from https://wdc.kugi.kyoto-u.ac.jp/ae_provisional/index.html.

Acknowledgments
This work has been supported by NASA projects 80NSSC21K0729, 80NSSC22K0752, 80NSSC20K1788, and NAS5-02099. We also acknowledge NSF support under Grant AGS-2019950. J. Liu was supported by NASA projects 80NSSC22K0749, 80NSSC22K0751, 80NSSC20K1314, and 80NSSC20K1316. We are grateful to NASA's CubeSat Launch Initiative for ELFIN's successful launch in the desired orbits. We acknowledge critical contributions of numerous ELFIN undergraduate student interns and volunteers. We gratefully acknowledge the SuperMAG collaborators (https://supermag.jhuapl.edu/info/?page=acknowledgement).

References

Amm, O., & Viljanen, A. (1999). Ionospheric disturbance magnetic field continuation from the ground to the ionosphere using spherical elementary current systems. *Earth Planets and Space*, *51*(6), 431–440. https://doi.org/10.1186/bf03352247

Angelopoulos, V., Artemyev, A., Phan, T. D., & Miyashita, Y. (2020). Near-Earth magnetotail reconnection powers space storms. *Nature Physics*, *16*(3), 317–321. https://doi.org/10.1038/s41567-019-0749-4

Angelopoulos, V., Cruce, P., Drozdov, A., Grimes, E. W., Hatzigeorgiu, N., King, D. A., et al. (2019). The space physics environment data analysis system (SPEDAS). *Space Science Reviews*, *215*(1), 9. https://doi.org/10.1007/s11214-018-0576-4

Angelopoulos, V., Kennel, C. F., Coroniti, F. V., Pellat, R., Kivelson, M. G., Walker, R. J., et al. (1994). Statistical characteristics of bursty bulk flow events. *Journal of Geophysical Research*, *99*(A11), 21257–21280. https://doi.org/10.1029/94JA01263

Angelopoulos, V., Kennel, C. F., Coroniti, F. V., Pellat, R., Spence, H. E., Kivelson, M. G., et al. (1993). Characteristics of ion flow in the quiet state of the inner plasma sheet. *Geophysical Research Letters*, *20*(16), 1711–1714. https://doi.org/10.1029/93GL00847

Angelopoulos, V., McFadden, J. P., Larson, D., Carlson, C. W., Mende, S. B., Frey, H., et al. (2008). Tail reconnection triggering substorm onset. *Science*, *321*(5891), 931–935. https://doi.org/10.1126/science.1160495

Angelopoulos, V., Sibeck, D., Carlson, C. W., McFadden, J. P., Larson, D., Lin, R. P., et al. (2008). First results from the THEMIS mission. *Space Science Reviews*, *141*(1–4), 453–476. https://doi.org/10.1007/s11214-008-9378-4

Angelopoulos, V., Tsai, E., Bingley, L., Shaffer, C., Turner, D. L., Runov, A., et al. (2020). The ELFIN mission. *Space Science Reviews*, *216*(5), 103. https://doi.org/10.1007/s11214-020-00721-7

Angelopoulos, V., Zhang, X.-J., Artemyev, A. V., Mourenas, D., Tsai, E., Wilkins, C., et al. (2023). Energetic electron precipitation driven by electromagnetic ion cyclotron waves from ELFIN's low altitude perspective. *Space Science Reviews*, *219*, 37. https://doi.org/10.1007/s11214-023-00984-w

Apatenkov, S. V., Sergeev, V. A., Kubyshkina, M. V., Nakamura, R., Baumjohann, W., Runov, A., et al. (2007). Multi-spacecraft observation of plasma dipolarization/injection in the inner magnetosphere. *Annales Geophysicae*, *25*(3), 801–814. https://doi.org/10.5194/angeo-25-801-2007

Artemyev, A. V., Angelopoulos, V., Runov, A., & Petrukovich, A. A. (2016). Properties of current sheet thinning at $x \sim 10$ to 12 R_E. *Journal of Geophysical Research: Space Physics*, *121*(7), 6718–6731. https://doi.org/10.1002/2016JA022779

Artemyev, A. V., Angelopoulos, V., Runov, A., & Petrukovich, A. A. (2019). Global view of current sheet thinning: Plasma pressure gradients and large-scale currents. *Journal of Geophysical Research: Space Physics*, *124*(1), 264–278. https://doi.org/10.1029/2018JA026113

Artemyev, A. V., Angelopoulos, V., Zhang, X.-J., Runov, A., Petrukovich, A., Nakamura, R., et al. (2022). Thinning of the magnetotail current sheet inferred from low-altitude observations of energetic electrons. *Journal of Geophysical Research: Space Physics*, *127*(10), e2022JA030705. https://doi.org/10.1029/2022JA030705

Artemyev, A. V., Lu, S., El-Alaoui, M., Lin, Y., Angelopoulos, V., Zhang, X.-J., et al. (2021). Configuration of the Earth's magnetotail current sheet. *Geophysical Research Letters*, *48*(6), e92153. https://doi.org/10.1029/2020GL092153

Artemyev, A. V., Neishtadt, A. I., & Angelopoulos, V. (2022). On the role of whistler-mode waves in electron interaction with dipolarizing flux bundles. *Journal of Geophysical Research: Space Physics*, *127*(4), e30265. https://doi.org/10.1029/2022JA030265

Auster, H. U., Glassmeier, K. H., Magnes, W., Aydogar, O., Baumjohann, W., Constantinescu, D., et al. (2008). The THEMIS fluxgate magnetometer. *Space Science Reviews*, *141*(1–4), 235–264. https://doi.org/10.1007/s11214-008-9365-9

Baker, D. N., Higbie, P. R., Hones, E. W., Jr., & Belian, R. D. (1978). High-resolution energetic particle measurements at 6.6 re 3. Low-energy electron anisotropies and short-term substorm predictions. *Journal of Geophysical Research*, *83*(A10), 4863–4868. https://doi.org/10.1029/JA083iA10p04863

Baker, D. N., & McPherron, R. L. (1990). Extreme energetic particle decreases near geostationary orbit: A manifestation of current diversion within the inner plasma sheet. *Journal of Geophysical Research*, *95*(A5), 6591–6599. https://doi.org/10.1029/JA095iA05p06591

Birn, J., Artemyev, A. V., Baker, D. N., Echim, M., Hoshino, M., & Zelenyi, L. M. (2012). Particle acceleration in the magnetotail and aurora. *Space Science Reviews*, *173*(1–4), 49–102. https://doi.org/10.1007/s11214-012-9874-4

Birn, J., & Hesse, M. (2013). The substorm current wedge in MHD simulations. *Journal of Geophysical Research: Space Physics*, *118*(6), 3364–3376. https://doi.org/10.1002/jgra.50187

Birn, J., Hesse, M., Haerendel, G., Baumjohann, W., & Shiokawa, K. (1999). Flow braking and the substorm current wedge. *Journal of Geophysical Research*, *104*(A9), 19895–19904. https://doi.org/10.1029/1999JA900173

Birn, J., Hesse, M., Nakamura, R., & Zaharia, S. (2013). Particle acceleration in dipolarization events. *Journal of Geophysical Research: Space Physics*, *118*(5), 1960–1971. https://doi.org/10.1002/jgra.50132

Birn, J., Hesse, M., & Runov, A. (2022). Electron anisotropies in magnetotail dipolarization events. *Frontiers in Astronomy and Space Sciences*, *9*, 908730. https://doi.org/10.3389/fspas.2022.908730

Birn, J., Liu, J., Runov, A., Kepko, L., & Angelopoulos, V. (2019). On the contribution of dipolarizing flux bundles to the substorm current wedge and to flux and energy transport. *Journal of Geophysical Research: Space Physics*, *124*(7), 5408–5420. https://doi.org/10.1029/2019JA026658

Birn, J., Runov, A., & Hesse, M. (2014). Energetic electrons in dipolarization events: Spatial properties and anisotropy. *Journal of Geophysical Research: Space Physics*, *119*(5), 3604–3616. https://doi.org/10.1002/2013JA019738

Bogott, F. H., & Mozer, F. S. (1973). Nightside energetic particle decreases at the synchronous orbit. *Journal of Geophysical Research*, *78*(34), 8119–8127. https://doi.org/10.1029/JA078i034p08119

Bonnell, J. W., Mozer, F. S., Delory, G. T., Hull, A. J., Ergun, R. E., Cully, C. M., et al. (2008). The electric field instrument (EFI) for THEMIS. *Space Science Reviews*, *141*(1–4), 303–341. https://doi.org/10.1007/s11214-008-9469-2

Bortnik, J., Thorne, R. M., O'Brien, T. P., Green, J. C., Strangeway, R. J., Shprits, Y. Y., & Baker, D. N. (2006). Observation of two distinct, rapid loss mechanisms during the 20 November 2003 radiation belt dropout event. *Journal of Geophysical Research*, *111*(A12), A12216. https://doi.org/10.1029/2006JA011802

Buchner, J., & Zelenyi, L. M. (1989). Regular and chaotic charged particle motion in magnetotaillike field reversals: 1. Basic theory of trapped motion. *Journal of Geophysical Research*, *94*(A9), 11821–11842. https://doi.org/10.1029/JA094iA09p11821

Chu, X., McPherron, R. L., Hsu, T.-S., & Angelopoulos, V. (2015). Solar cycle dependence of substorm occurrence and duration: Implications for onset. *Journal of Geophysical Research: Space Physics*, *120*(4), 2808–2818. https://doi.org/10.1002/2015JA021104

Delcourt, D. C., Sauvaud, J. A., Martin, R. F., & Moore, T. E. (1995). Gyrophase effects in the centrifugal impulse model of particle motion in the magnetotail. *Journal of Geophysical Research*, *100*(A9), 17211–17220. https://doi.org/10.1029/95JA00657

Donovan, E., Liu, W., Liang, J., Spanswick, E., Voronkov, I., Connors, M., et al. (2008). Simultaneous THEMIS in situ and auroral observations of a small substorm. *Geophysical Research Letters*, *35*(17), L17S18. https://doi.org/10.1029/2008GL033794

Dubyagin, S., Ganushkina, N. Y., & Sergeev, V. (2018). Formation of 30 KeV proton isotropic boundaries during geomagnetic storms. *Journal of Geophysical Research: Space Physics*, *123*(5), 3436–3459. https://doi.org/10.1002/2017JA024587

Dubyagin, S., Sergeev, V. A., & Kubyshkina, M. V. (2002). On the remote sensing of plasma sheet from low-altitude spacecraft. *Journal of Atmospheric and Solar-Terrestrial Physics*, *64*(5–6), 567–572. https://doi.org/10.1016/S1364-6826(02)00014-7

Engebretson, M. J., Hughes, W. J., Alford, J. L., Zesta, E., Cahill, L. J., Arnoldy, R. L., & Reeves, G. D. (1995). Magnetometer array for cusp and cleft studies observations of the spatial extent of broadband ULF magnetic pulsations at cusp/cleft latitudes. *Journal of Geophysical Research*, *100*(A10), 19371–19386. https://doi.org/10.1029/95JA00768

Ergun, R. E., Goodrich, K. A., Stawarz, J. E., Andersson, L., & Angelopoulos, V. (2015). Large-amplitude electric fields associated with bursty bulk flow braking in the Earth's plasma sheet. *Journal of Geophysical Research: Space Physics*, *120*(3), 1832–1844. https://doi.org/10.1002/2014JA020165

Eshetu, W. W., Lyon, J. G., Hudson, M. K., & Wiltberger, M. J. (2018). Pitch angle scattering of energetic electrons by BBFs. *Journal of Geophysical Research: Space Physics*, *123*(11), 9265–9274. https://doi.org/10.1029/2018JA025788

Eshetu, W. W., Lyon, J. G., Hudson, M. K., & Wiltberger, M. J. (2019). Simulations of electron energization and injection by BBFs using high-resolution LFM MHD fields. *Journal of Geophysical Research: Space Physics*, *124*(2), 1222–1238. https://doi.org/10.1029/2018JA025789

Fennell, J., Roeder, J., Spence, H., Singer, H., Korth, A., Grande, M., & Vampola, A. (1996). CRRES observations of particle flux dropout events. *Advances in Space Research*, *18*(8), 217–228. https://doi.org/10.1016/0273-1177(95)00991-4

Forsyth, C., Rae, I. J., Coxon, J. C., Freeman, M. P., Jackman, C. M., Gjerloev, J., & Fazakerley, A. N. (2015). A new technique for determining substorm onsets and phases from indices of the electrojet (SOPHIE). *Journal of Geophysical Research: Space Physics*, *120*(12), 10592–10606. https://doi.org/10.1002/2015JA021343

Fu, H., Grigorenko, E. E., Gabrielse, C., Liu, C., Lu, S., Hwang, K. J., et al. (2020). Magnetotail dipolarization fronts and particle acceleration: A review. *Science China Earth Sciences*, *63*(2), 235–256. https://doi.org/10.1007/s11430-019-9551-y

Fu, H. S., Khotyaintsev, Y. V., Vaivads, A., André, M., Sergeev, V. A., Huang, S. Y., et al. (2012). Pitch angle distribution of suprathermal electrons behind dipolarization fronts: A statistical overview. *Journal of Geophysical Research*, *117*(A12), 12221. https://doi.org/10.1029/2012JA018141

Gabrielse, C., Angelopoulos, V., Harris, C., Artemyev, A., Kepko, L., & Runov, A. (2017). Extensive electron transport and energization via multiple, localized dipolarizing flux bundles. *Journal of Geophysical Research*, *122*(5), 5059–5076. https://doi.org/10.1002/2017JA023981

Gabrielse, C., Spanswick, E., Artemyev, A., Nishimura, Y., Runov, A., Lyons, L., et al. (2019). Utilizing the heliophysics/geospace system observatory to understand particle injections: Their scale sizes and propagation directions. *Journal of Geophysical Research: Space Physics*, *124*(7), 5584–5609. https://doi.org/10.1029/2018JA025588

Gallardo-Lacourt, B., Wing, S., Kepko, L., Gillies, D. M., Spanswick, E. L., Roy, E. A., & Donovan, E. F. (2022). Polar cap boundary identification using redline optical data and DMSP satellite particle data. *Journal of Geophysical Research: Space Physics*, *127*(5), e30148. https://doi.org/10.1029/2021JA030148

Ganushkina, N. Y., Liemohn, M. W., & Dubyagin, S. (2018). Current systems in the earth's magnetosphere. *Reviews of Geophysics*, *56*(2), 309–332. https://doi.org/10.1002/2017RG000590

Ganushkina, N. Y., Liemohn, M. W., Kubyshkina, M. V., Ilie, R., & Singer, H. J. (2010). Distortions of the magnetic field by storm-time current systems in Earth's magnetosphere. *Annales Geophysicae*, *28*(1), 123–140. https://doi.org/10.5194/angeo-28-123-2010

Gillies, D. M., Donovan, E., Hampton, D., Liang, J., Connors, M., Nishimura, Y., et al. (2019). First observations from the trex spectrograph: The optical spectrum of steve and the picket fence phenomena. *Geophysical Research Letters*, *46*(13), 7207–7213. https://doi.org/10.1029/2019GL083272

Gjerloev, J. W. (2012). The supermag data processing technique. *Journal of Geophysical Research*, *117*(A9), A09213. https://doi.org/10.1029/2012JA017683

Gkioulidou, M., Ohtani, S., Mitchell, D. G., Ukhorskiy, A. Y., Reeves, G. D., Turner, D. L., et al. (2015). Spatial structure and temporal evolution of energetic particle injections in the inner magnetosphere during the 14 July 2013 substorm event. *Journal of Geophysical Research*, *120*(3), 1924–1938. https://doi.org/10.1002/2014JA020872

Gkioulidou, M., Wang, C.-P., Lyons, L. R., & Wolf, R. A. (2009). Formation of the Harang reversal and its dependence on plasma sheet conditions: Rice convection model simulations. *Journal of Geophysical Research*, *114*(A7), A07204. https://doi.org/10.1029/2008JA013955

Heikkila, W. J., & Winningham, J. D. (1971). Penetration of magnetosheath plasma to low altitudes through the dayside magnetospheric cusps. *Journal of Geophysical Research*, *76*(4), 883–891. https://doi.org/10.1029/JA076i004p00883

Huang, C.-S., Foster, J. C., Reeves, G. D., Le, G., Frey, H. U., Pollock, C. J., & Jahn, J.-M. (2003). Periodic magnetospheric substorms: Multiple space-based and ground-based instrumental observations. *Journal of Geophysical Research*, *108*(A11), 1411. https://doi.org/10.1029/2003JA009992

Iijima, T., & Potemra, T. A. (1978). Large-scale characteristics of field-aligned currents associated with substorms. *Journal of Geophysical Research*, *83*(A2), 599–615. https://doi.org/10.1029/JA083iA02p00599

Ilie, R., Ganushkina, N., Toth, G., Dubyagin, S., & Liemohn, M. W. (2015). Testing the magnetotail configuration based on observations of low-altitude isotropic boundaries during quiet times. *Journal of Geophysical Research: Space Physics*, *120*(12), 10557–10573. https://doi.org/10.1002/2015JA021858

Kennel, C. F., & Petschek, H. E. (1966). Limit on stably trapped particle fluxes. *Journal of Geophysical Research*, *71*, 1–28. https://doi.org/10.1029/jz071i001p00001

Kepko, L., Glassmeier, K. H., Slavin, J. A., & Sundberg, T. (2015). Substorm current wedge at earth and Mercury. In *Magnetotails in the solar system* (Vol. 207, pp. 361–372). https://doi.org/10.1002/9781118842324.ch21

Kepko, L., McPherron, R. L., Amm, O., Apatenkov, S., Baumjohann, W., Birn, J., et al. (2014). Substorm current wedge revisited. *Space Science Reviews*, *190*(1–4), 1–46. https://doi.org/10.1007/s11214-014-0124-9

Kubyshkina, M., Sergeev, V., Tsyganenko, N., Angelopoulos, V., Runov, A., Donovan, E., et al. (2011). Time-dependent magnetospheric configuration and breakup mapping during a substorm. *Journal of Geophysical Research*, *116*(A5), A00I27. https://doi.org/10.1029/2010JA015882

Kubyshkina, M., Sergeev, V., Tsyganenko, N., Angelopoulos, V., Runov, A., Singer, H., et al. (2009). Toward adapted time-dependent magnetospheric models: A simple approach based on tuning the standard model. *Journal of Geophysical Research*, *114*(A1), A00C21. https://doi.org/10.1029/2008JA013547

Kubyshkina, M., Sergeev, V. A., Tsyganenko, N. A., & Zheng, Y. (2019). Testing efficiency of empirical, adaptive, and global MHD magnetospheric models to represent the geomagnetic field in a variety of conditions. *Space Weather*, *17*(5), 672–686. https://doi.org/10.1029/2019SW002157

Liang, J., Donovan, E., Spanswick, E., & Angelopoulos, V. (2013). Multiprobe estimation of field line curvature radius in the equatorial magnetosphere and the use of proton precipitations in magnetosphere-ionosphere mapping. *Journal of Geophysical Research: Space Physics*, *118*(8), 4924–4945. https://doi.org/10.1002/jgra.50454

Liu, J., Angelopoulos, V., Runov, A., & Zhou, X.-Z. (2013). On the current sheets surrounding dipolarizing flux bundles in the magnetotail: The case for wedgelets. *Journal of Geophysical Research: Space Physics*, *118*(5), 2000–2020. https://doi.org/10.1002/jgra.50092

Liu, J., Angelopoulos, V., Zhang, X.-J., Turner, D. L., Gabrielse, C., Runov, A., et al. (2016). Dipolarizing flux bundles in the cis-geosynchronous magnetosphere: Relationship between electric fields and energetic particle injections. *Journal of Geophysical Research: Space Physics*, *121*(2), 1362–1376. https://doi.org/10.1002/2015JA021691

Liu, J., Higuchi, T., Lyons, L. R., Ohtani, S., Wu, J., Zou, Y., et al. (2022). The occurrence of embedded region 1 and 2 currents depends on geomagnetic activity level. *Journal of Geophysical Research: Space Physics*, *127*(11), e2022JA030539. https://doi.org/10.1029/2022JA030539

Liu, J., Lyons, L. R., Wang, C.-P., Ma, Y., Strangeway, R. J., Zhang, Y., et al. (2021). Embedded regions 1 and 2 field-aligned currents: Newly recognized from low-altitude spacecraft observations. *Journal of Geophysical Research: Space Physics*, *126*(6), e29207. https://doi.org/10.1029/2021JA029207

Lotoániu, P. T., Califf, S., Redmon, R. J., & Singer, H. J. (2020). Chapter 21—Magnetic field observations from the goes-r series. In S. J. Goodman, T. J. Schmit, J. Daniels, & R. J. Redmon (Eds.), *The goes-r series* (pp. 251–259). Elsevier. https://doi.org/10.1016/B978-0-12-814327-8.00021-4

Lu, S., Pritchett, P. L., Angelopoulos, V., & Artemyev, A. V. (2018). Formation of dawn-dusk asymmetry in Earth's magnetotail thin current sheet: A three-dimensional particle-in-cell simulation. *Journal of Geophysical Research: Space Physics*, *123*(4), 2801–2814. https://doi.org/10.1002/2017JA025095

Lukin, A. S., Artemyev, A. V., & Petrukovich, A. A. (2021). On application of stochastic differential equations for simulation of nonlinear wave-particle resonant interactions. *Physics of Plasmas*, *28*(9), 092904. https://doi.org/10.1063/5.0058054

Lyons, L. R., Nishimura, Y., Donovan, E., & Angelopoulos, V. (2013). Distinction between auroral substorm onset and traditional ground magnetic onset signatures. *Journal of Geophysical Research: Space Physics*, *118*(7), 4080–4092. https://doi.org/10.1002/jgra.50384

Mann, I. R., Milling, D. K., Rae, I. J., Ozeke, L. G., Kale, A., Kale, Z. C., et al. (2008). The upgraded CARISMA magnetometer array in the THEMIS era. *Space Science Reviews*, *141*(1–4), 413–451. https://doi.org/10.1007/s11214-008-9457-6

Mauk, B. H., & Meng, C. I. (1987). Plasma injection during substorms. *Physica Scripta Volume T*, *18*, 128–139. https://doi.org/10.1088/0031-8949/1987/T18/014

McFadden, J. P., Carlson, C. W., Larson, D., Ludlam, M., Abiad, R., Elliott, B., et al. (2008). The THEMIS ESA plasma instrument and in-flight calibration. *Space Science Reviews*, *141*(1–4), 277–302. https://doi.org/10.1007/s11214-008-9440-2

McPherron, R. L. (1972). Substorm related changes in the geomagnetic tail: The growth phase. *Planatary Space Science*, *20*(9), 1521–1539. https://doi.org/10.1016/0032-0633(72)90054-2

McPherron, R. L., & Chu, X. (2017). The mid-latitude positive bay and the MPB index of substorm activity. *Space Science Reviews*, *206*(1–4), 91–122. https://doi.org/10.1007/s11214-016-0316-6

McPherron, R. L., Russell, C. T., & Aubry, M. P. (1973). Satellite studies of magnetospheric substorms on august 15, 1968: 9. Phenomenological model for substorms. *Journal of Geophysical Research*, *78*(16), 3131–3149. https://doi.org/10.1029/JA078i016p03131

Mende, S. B., Angelopoulos, V., Frey, H. U., Harris, S., Donovan, E., Jackel, B., et al. (2007). Determination of substorm onset timing and location using the THEMIS ground based observatories. *Geophysical Research Letters*, *34*(17), 17108. https://doi.org/10.1029/2007GL030850

Merkin, V. G., Panov, E. V., Sorathia, K. A., & Ukhorskiy, A. Y. (2019). Contribution of bursty bulk flows to the global dipolarization of the magnetotail during an isolated substorm. *Journal of Geophysical Research: Space Physics*, *124*(11), 8647–8668. https://doi.org/10.1029/2019JA026872

Moldwin, M. B., Thomsen, M. F., Bame, S. J., McComas, D. J., Birn, J., Reeves, G. D., et al. (1995). Flux dropouts of plasma and energetic particles at geosynchronous orbit during large geomagnetic storms: Entry into the lobes. *Journal of Geophysical Research*, *100*(A5), 8031–8043. https://doi.org/10.1029/94JA03025

Morley, S. K., Friedel, R. H. W., Cayton, T. E., & Noveroske, E. (2010). A rapid, global and prolonged electron radiation belt dropout observed with the global positioning system constellation. *Geophysical Research Letters*, *37*(6), 6102. https://doi.org/10.1029/2010GL042772

Newell, P. T., & Gjerloev, J. W. (2011). Evaluation of supermag auroral electrojet indices as indicators of substorms and auroral power. *Journal of Geophysical Research*, *116*(A12), A12211. https://doi.org/10.1029/2011JA016779

Newell, P. T., & Meng, C.-I. (1992). Mapping the dayside ionosphere to the magnetosphere according to particle precipitation characteristics. *Geophysical Research Letters*, *19*(6), 609–612. https://doi.org/10.1029/92GL00404

Newell, P. T., Sergeev, V. A., Bikkuzina, G. R., & Wing, S. (1998). Characterizing the state of the magnetosphere: Testing the ion precipitation maxima latitude (b2i) and the ion isotropy boundary. *Journal of Geophysical Research*, *103*(A3), 4739–4746. https://doi.org/10.1029/97JA03622

Ni, B., Thorne, R. M., Meredith, N. P., Horne, R. B., & Shprits, Y. Y. (2011). Resonant scattering of plasma sheet electrons leading to diffuse auroral precipitation: 2. Evaluation for whistler mode chorus waves. *Journal of Geophysical Research*, *116*(A4), 4219. https://doi.org/10.1029/2010JA016233

Ni, B., Thorne, R. M., Shprits, Y. Y., Orlova, K. G., & Meredith, N. P. (2011). Chorus-driven resonant scattering of diffuse auroral electrons in nondipolar magnetic fields. *Journal of Geophysical Research*, *116*(A6), 6225. https://doi.org/10.1029/2011JA016453

Ni, B., Thorne, R. M., Zhang, X., Bortnik, J., Pu, Z., Xie, L., et al. (2016). Origins of the Earth's diffuse auroral precipitation. *Space Science Reviews*, *200*(1–4), 205–259. https://doi.org/10.1007/s11214-016-0234-7

Onsager, T. G., & Mukai, T. (1995). Low altitude signature of the plasma sheet boundary layer: Observations and model. *Geophysical Research Letters*, *22*(7), 855–858. https://doi.org/10.1029/95GL00304

Onsager, T. G., Rostoker, G., Kim, H.-J., Reeves, G. D., Obara, T., Singer, H. J., & Smithtro, C. (2002). Radiation belt electron flux dropouts: Local time, radial, and particle-energy dependence. *Journal of Geophysical Research*, *107*(A11), 1382. https://doi.org/10.1029/2001JA000187

Orlova, K. G., & Shprits, Y. Y. (2010). Dependence of pitch-angle scattering rates and loss timescales on the magnetic field model. *Geophysical Research Letters*, *37*(5), 5105. https://doi.org/10.1029/2009GL041639

Panov, E. V., Baumjohann, W., Wolf, R. A., Nakamura, R., Angelopoulos, V., Weygand, J. M., & Kubyshkina, M. V. (2016). Magnetotail energy dissipation during an auroral substorm. *Nature Physics*, *12*, 1158–1163. https://doi.org/10.1038/nphys3879

Petrukovich, A. A., Baumjohann, W., Nakamura, R., Runov, A., Balogh, A., & Rème, H. (2007). Thinning and stretching of the plasma sheet. *Journal of Geophysical Research*, *112*(A10), 10213. https://doi.org/10.1029/2007JA012349

Runov, A., Angelopoulos, V., Artemyev, A. V., Weygand, J. M., Lu, S., Lin, Y., & Zhang, X. J. (2021). Global and local processes of thin current sheet formation during substorm growth phase. *Journal of Atmospheric and Solar-Terrestrial Physics*, *220*, 105671. https://doi.org/10.1016/j.jastp.2021.105671

Runov, A., Angelopoulos, V., Gabrielse, C., Liu, J., Turner, D. L., & Zhou, X.-Z. (2015). Average thermodynamic and spectral properties of plasma in and around dipolarizing flux bundles. *Journal of Geophysical Research*, *120*(6), 4369–4383. https://doi.org/10.1002/2015JA021166

Runov, A., Angelopoulos, V., Gabrielse, C., Zhou, X.-Z., Turner, D., & Plaschke, F. (2013). Electron fluxes and pitch-angle distributions at dipolarization fronts: THEMIS multipoint observations. *Journal of Geophysical Research*, *118*(2), 744–755. https://doi.org/10.1002/jgra.50121

Russell, C. T., Chi, P. J., Dearborn, D. J., Ge, Y. S., Kuo-Tiong, B., Means, J. D., et al. (2008). THEMIS ground-based magnetometers. *Space Science Reviews*, *141*(1–4), 389–412. https://doi.org/10.1007/s11214-008-9337-0

Sauvaud, J.-A., & Winckler, J. R. (1980). Dynamics of plasma, energetic particles, and fields near synchronous orbit in the nighttime sector during magnetospheric substorms. *Journal of Geophysical Research*, *85*(A5), 2043–2056. https://doi.org/10.1029/JA085iA05p02043

Sergeev, V. A., Angelopoulos, V., & Nakamura, R. (2012). Recent advances in understanding substorm dynamics. *Geophysical Research Letters*, *39*(5), L05101. https://doi.org/10.1029/2012GL050859

Sergeev, V. A., Bosinger, T., Belian, R. D., Reeves, G. D., & Cayton, T. E. (1992). Drifting holes in the energetic electron flux at geosynchronous orbit following substorm onset. *Journal of Geophysical Research*, *97*(A5), 6541–6548. https://doi.org/10.1029/92JA00182

Sergeev, V. A., Chernyaev, I. A., Dubyagin, S. V., Miyashita, Y., Angelopoulos, V., Boakes, P. D., et al. (2012). Energetic particle injections to geostationary orbit: Relationship to flow bursts and magnetospheric state. *Journal of Geophysical Research*, *117*(A10), A10207. https://doi.org/10.1029/2012JA017773

Sergeev, V. A., Malkov, M., & Mursula, K. (1993). Testing the isotropic boundary algorithm method to evaluate the magnetic field configuration in the tail. *Journal of Geophysical Research*, *98*(A5), 7609–7620. https://doi.org/10.1029/92JA02587

Sergeev, V. A., Nishimura, Y., Kubyshkina, M., Angelopoulos, V., Nakamura, R., & Singer, H. (2012). Magnetospheric location of the equatorward prebreakup arc. *Journal of Geophysical Research*, *117*(A1), A01212. https://doi.org/10.1029/2011JA017154

Sergeev, V. A., Sazhina, E. M., Tsyganenko, N. A., Lundblad, J. A., & Soraas, F. (1983). Pitch-angle scattering of energetic protons in the magnetotail current sheet as the dominant source of their isotropic precipitation into the nightside ionosphere. *Planatary Space Science*, *31*(10), 1147–1155. https://doi.org/10.1016/0032-0633(83)90103-4

Sergeev, V. A., & Tsyganenko, N. A. (1982). Energetic particle losses and trapping boundaries as deduced from calculations with a realistic magnetic field model. *Planatary Space Science*, *30*(10), 999–1006. https://doi.org/10.1016/0032-0633(82)90149-0

Sergeev, V. A., Tsyganenko, N. A., Angelopoulos, V., Runov, A. V., & Singer, H. J. (2018). Magnetotail configuration during a steady convection event as observed by low-altitude and magnetospheric spacecraft. *Journal of Geophysical Research: Space Physics*, *123*(10), 8390–8406. https://doi.org/10.1029/2018JA025867

Shen, Y. (2023). Dataset for "Energetic electron flux dropouts measured by ELFIN in the ionospheric projection of the plasma sheet" [Dataset]. Zenodo. https://doi.org/10.5281/zenodo.8136713

Shen, Y., Artemyev, A., Vasko, I., Zhang, X.-J., Angelopoulos, V., An, X., & Runov, A. (2022). Energetic electron scattering by kinetic Alfvén waves at strong magnetic field gradients of dipolarization front. *Physics of Plasmas*, *29*(8), 082901. https://doi.org/10.1063/5.0096338

Shen, Y., Artemyev, A. V., Zhang, X.-J., Zou, Y., Angelopoulos, V., Vasko, I., et al. (2023). Contribution of kinetic Alfvén waves to energetic electron precipitation from the plasma sheet during a substorm. *Journal of Geophysical Research: Space Physics*, *128*(4), e2023JA031350. https://doi.org/10.1029/2023JA031350

Shiokawa, K., Haerendel, G., & Baumjohann, W. (1998). Azimuthal pressure gradient as driving force of substorm currents. *Geophysical Research Letters*, *25*(7), 959–962. https://doi.org/10.1029/98GL00540

Shprits, Y. Y., Thorne, R. M., Friedel, R., Reeves, G. D., Fennell, J., Baker, D. N., & Kanekal, S. G. (2006). Outward radial diffusion driven by losses at magnetopause. *Journal of Geophysical Research*, *111*(A11), 11214. https://doi.org/10.1029/2006JA011657

Smets, R., Delcourt, D., Sauvaud, J. A., & Koperski, P. (1999). Electron pitch angle distributions following the dipolarization phase of a substorm: Interball-tail observations and modeling. *Journal of Geophysical Research*, *104*(A7), 14571–14576. https://doi.org/10.1029/1998JA900162

Smith, M. F., & Lockwood, M. (1996). Earth's magnetospheric cusps. *Reviews of Geophysics*, *34*(2), 233–260. https://doi.org/10.1029/96RG00893

Stephens, G. K., & Sitnov, M. I. (2021). Concurrent empirical magnetic reconstruction of storm and substorm spatial scales using data mining and virtual spacecraft. *Frontiers in Physics*, *9*, 210. https://doi.org/10.3389/fphy.2021.653111

Stephens, G. K., Sitnov, M. I., Korth, H., Tsyganenko, N. A., Ohtani, S., Gkioulidou, M., & Ukhorskiy, A. Y. (2019). Global empirical picture of magnetospheric substorms inferred from Multimission magnetometer data. *Journal of Geophysical Research: Space Physics*, *124*(2), 1085–1110. https://doi.org/10.1029/2018JA025843

Stephens, G. K., Sitnov, M. I., Ukhorskiy, A. Y., Roelof, E. C., Tsyganenko, N. A., & Le, G. (2016). Empirical modeling of the storm time innermost magnetosphere using Van Allen Probes and THEMIS data: Eastward and banana currents. *Journal of Geophysical Research: Space Physics*, *121*(1), 157–170. https://doi.org/10.1002/2015JA021700

Stephens, G. K., Sitnov, M. I., Weigel, R. S., Turner, D. L., Tsyganenko, N. A., Rogers, A. J., et al. (2023). Global structure of magnetotail reconnection revealed by mining space magnetometer data. *Journal of Geophysical Research: Space Physics*, *128*(2), e2022JA031066. https://doi.org/10.1029/2022JA031066

Tanskanen, E., Pulkkinen, T. I., Koskinen, H. E. J., & Slavin, J. A. (2002). Substorm energy budget during low and high solar activity: 1997 and 1999 compared. *Journal of Geophysical Research*, *107*(A6), 1086. https://doi.org/10.1029/2001JA900153

Tsyganenko, N. A. (1995). Modeling the Earth's magnetospheric magnetic field confined within a realistic magnetopause. *Journal of Geophysical Research*, *100*(A4), 5599–5612. https://doi.org/10.1029/94JA03193

Tsyganenko, N. A. (2002). A model of the near magnetosphere with a dawn-dusk asymmetry 1. Mathematical structure. *Journal of Geophysical Research*, *107*(A8), SMP12-1–SMP12-15. https://doi.org/10.1029/2001JA000219

Tsyganenko, N. A., & Andreeva, V. A. (2016). An empirical RBF model of the magnetosphere parameterized by interplanetary and ground-based drivers. *Journal of Geophysical Research: Space Physics*, *121*(11), 10. https://doi.org/10.1002/2016JA023217

Tsyganenko, N. A., Andreeva, V. A., Sitnov, M. I., Stephens, G. K., Gjerloev, J. W., Chu, X., & Troshichev, O. A. (2021). Reconstructing substorms via historical data mining: Is it really feasible? *Journal of Geophysical Research: Space Physics*, *126*(10), e2021JA029604. https://doi.org/10.1029/2021JA029604

Tsyganenko, N. A., & Sitnov, M. I. (2005). Modeling the dynamics of the inner magnetosphere during strong geomagnetic storms. *Journal of Geophysical Research*, *110*(A3), A03208. https://doi.org/10.1029/2004JA010798

Tsyganenko, N. A., & Stern, D. P. (1996). Modeling the global magnetic field of the large-scale Birkeland current systems. *Journal of Geophysical Research*, *101*(A12), 27187–27198. https://doi.org/10.1029/96JA02735

Turner, D. L., Fennell, J. F., Blake, J. B., Clemmons, J. H., Mauk, B. H., Cohen, I. J., et al. (2016). Energy limits of electron acceleration in the plasma sheet during substorms: A case study with the magnetospheric multiscale (MMS) mission. *Geophysical Research Letters*, *43*(15), 7785–7794. https://doi.org/10.1002/2016GL069691

Turner, D. L., Shprits, Y., Hartinger, M., & Angelopoulos, V. (2012). Explaining sudden losses of outer radiation belt electrons during geomagnetic storms. *Nature Physics*, *8*(3), 208–212. https://doi.org/10.1038/nphys2185

Ukhorskiy, A. Y., Sorathia, K. A., Merkin, V. G., Crabtree, C., Fletcher, A. C., Malaspina, D. M., & Schwartz, S. J. (2022). Cross-scale energy cascade powered by magnetospheric convection. *Scientific Reports*, *12*(1), 4446. https://doi.org/10.1038/s41598-022-08038-x

Vasyliunas, V. M. (1970). Mathematical models of magnetospheric convection and its coupling to the ionosphere. In B. M. McCormack & A. Renzini (Eds.), *Particles and field in the magnetosphere* (Vol. 17, p. 60). https://doi.org/10.1007/978-94-010-3284-1-6

Walsh, B. M., Collier, M. R., Atz, E., Billingsley, L., Broll, J. M., Connor, H. K., et al. (2021). The cusp plasma imaging detector (CuPID) CubeSat observatory: Mission overview. *Journal of Geophysical Research: Space Physics*, *126*(4), e29015. https://doi.org/10.1029/2020JA029015

Weygand, J. M. (2009a). Spherical elementary currents systems (SECS) technique equivalent ionospheric currents (EICs) derived at 10 sec resolution in geographic coordinates [Dataset]. University of California. https://doi.org/10.21978/p8d62b

Weygand, J. M. (2009b). Spherical elementary currents systems (SECS) technique equivalent ionospheric currents (EICs) derived at 10 sec resolution in geographic coordinates [Dataset]. University of California. https://doi.org/10.21978/p8pp8x

Weygand, J. M., Amm, O., Viljanen, A., Angelopoulos, V., Murr, D., Engebretson, M. J., et al. (2011). Application and validation of the spherical elementary currents systems technique for deriving ionospheric equivalent currents with the North American and Greenland ground magnetometer arrays. *Journal of Geophysical Research*, *116*(A3), A03305. https://doi.org/10.1029/2010JA016177

Wiltberger, M., Merkin, V., Lyon, J. G., & Ohtani, S. (2015). High-resolution global magnetohydrodynamic simulation of bursty bulk flows. *Journal of Geophysical Research: Space Physics*, *120*(6), 4555–4566. https://doi.org/10.1002/2015JA021080

Wing, S., & Zhang, Y. L. (2015). The nightside magnetic field line open-closed boundary and polar rain electron energy-latitude dispersion. *Annales Geophysicae*, *33*(1), 39–46. https://doi.org/10.5194/angeo-33-39-2015

Winningham, J. D., & Heikkila, W. J. (1974). Polar cap auroral electron fluxes observed with Isis 1. *Journal of Geophysical Research*, *79*(7), 949–957. https://doi.org/10.1029/JA079i007p00949

Xiang, Z., Tu, W., Li, X., Ni, B., Morley, S. K., & Baker, D. N. (2017). Understanding the mechanisms of radiation belt dropouts observed by Van Allen Probes. *Journal of Geophysical Research: Space Physics*, *122*(10), 9858–9879. https://doi.org/10.1002/2017JA024487

Xing, X., Lyons, L. R., Angelopoulos, V., Larson, D., McFadden, J., Carlson, C., et al. (2009). Azimuthal plasma pressure gradient in quiet time plasma sheet. *Geophysical Research Letters*, *36*(14), L14105. https://doi.org/10.1029/2009GL038881

Yang, J., Toffoletto, F. R., Wolf, R. A., Sazykin, S., Ontiveros, P. A., & Weygand, J. M. (2012). Large-scale current systems and ground magnetic disturbance during deep substorm injections. *Journal of Geophysical Research*, *117*(A4), A04223. https://doi.org/10.1029/2011JA017415

Yue, C., Wang, C.-P., Nishimura, Y., Murphy, K. R., Xing, X., Lyons, L., et al. (2015). Empirical modeling of 3-D force-balanced plasma and magnetic field structures during substorm growth phase. *Journal of Geophysical Research: Space Physics*, *120*(8), 6496–6513. https://doi.org/10.1002/2015JA021226

Yue, C., Wang, C.-P., Zaharia, S. G., Xing, X., & Lyons, L. (2013). Empirical modeling of plasma sheet pressure and three-dimensional force-balanced magnetospheric magnetic field structure: 2. Modeling. *Journal of Geophysical Research: Space Physics*, *118*(10), 6166–6175. https://doi.org/10.1002/2013JA018943